Theses and Dissertations

2016

Design, Manufacture and Prototyping of a Hydrokinetic Turbine Unit for River Application

Nick Oblas
Lehigh University

Follow this and additional works at: http://preserve.lehigh.edu/etd

Part of the Mechanical Engineering Commons

Design, Manufacture and Prototyping of a Hydrokinetic Turbine Unit for River
Application

by

Nick Oblas

A Thesis

Presented to the Graduate and Research Committee

of Lehigh University

in Candidacy for the Degree of

Master of Sciences

in

Mechanical Engineering

Lehigh University

December, 2015

Thesis is accepted and approved in partial fulfillment of the requirements for the degree of Master of Science in Mechanical Engineering

Nick Oblas
Design, Manufacturing and Prototyping of a Hydrokinetic Turbine Unit for River Application

_____

Approved Date

                                                                  _____

Dr. Alparslan Oztekin
Thesis Director

                                                                  _____

Dr. Gary Harlow

Table of Contents

List of Figures

List of Tables

Acknowledgements

The author would like to express his greatest appreciation to Dr. Oztekin for the guidance and encouragement he has provided during the author's pursuit of a Master of Science not only through research efforts but through the continued growth in academia.

Many thanks to the support and collaborative efforts of Dr. Jacob Riglin, Dr. Chris Schleicher and Fred Cart. Finally, the author is truly grateful for the love and encouragement of his parents, Stephen and Stephanie Oblas.

Nomenclature

A	area, m^2	**Greek Symbols**	
B	channel width, m	*β*	relative angle, °
c	damping resistance, 1/m	*λ*	tip speed ratio
D	diameter, m	*μ*	dynamic viscosity, Pa-s
d	depth, m	*v*	kinematic viscosity, m^2/s
F	forces, N	*ρ*	density, kg/m^3
Fr	Froude number	*ω*	angular velocity, 1/s
g	gravity, m/s^2	$\widetilde{\omega}$	normalized vorticity
m	meridional length, m		
$\dot{m}$	mass flow, kg/s	**Subscripts**	
P	pressure, Pa		
Re	Reynolds number	*B*	blades
s	cylinder cross section width, m	*D*	drag
t	time, s	*L*	lift
T	thrust, N	*m*	at the mean value
U	velocity, m/s	*max*	maximum value
$\widetilde{U}$	normalized velocity	*m*	at the mean value
V	volume, m^3	*max*	maximum value
$\dot{W}$	power, W	*max*	maximum value
		T	turbulent / thrust
		t	at the tip
		∞	freestream

Abstract

Hydrokinetic technology has a long history as a viable long term renewable energy. It has outpaced wind energy production in the U.S. due to the largely unpredictable and inconsistent nature of wind while most hydrokinetic technology operates in near constant flow conditions. These conditions are created through the construction of massive dams, causing intense and mostly irreversible damage to the surrounding area. Submerged hydrokinetic turbine systems are an alternative that has the potential to produce smaller quantities of electricity in far more locations.

Energy production systems that produce less than 100kW are considered micro-hydrokinetic systems. This level of production is ideal for isolated supplementary, emergency, and off-grid power generation. The design focus was to create a micro-hydrokinetic turbine system to generate 250W of continuous power that could be transported by a small team.

As numerical models and optimization techniques were applied to the turbine design, the design necessitated a shift towards increasing manufacturability while maintaining peak performance. By analyzing the CFD and optimization data of ideal conditions, critical and noncritical design locations can be determined. These critical and non critical locations were used to ultimately determine the way in which each component was to be manufactured. These modifications and manufacturing methods were imposed in the final design of the prototype and the influence of each was compared with ideal geometric conditions of the turbine.

Chapter 1: Introduction

Motivation

In 2014 the U.S. produced 722 GWhrs of hydroelectric power, accounting for 25% of the renewable energy produced and 2.5% of total energy produced in the U.S. that year [1]. Much of that power is harvested from large hydroelectric facilities that have massive local environmental impact. Micro-hydrokinetic devices are a far less detrimental alternative to large scale hydroelectric energy production. For this design, an optimal flow speed of 1.5m/s with a depth of at least 2m is needed for the ideal conditions in which it was tested. While ideal locations for large hydroelectric facilities are scarce, there are an estimated 40,000 suitable sites in the U.S. that could be outfitted with a system of similar design [2]. Determining an economical solution for most micro-hydrokinetic turbine applications remains a barrier to market. This design provides a proof of concept for the targeted suitable application sites in the U.S.

Components of a Hydrokinetic Turbine

The hydrokinetic turbine consists of five critical design components that have a large effect on the overall power produced by a specific turbine geometry. The first design component is the runner. In general, the runner consists of blades connected to a central hub that ultimately provides the shaft to transmit torque to the system. The diffuser design needs to be carefully considered due to the effect is has on both power efficiency and downstream thrust generated. This implies that there is an optimum design for a given flow rate, or a maximum increase in power efficiency with minimal increases in thrust. The structural integrity of the diffuser is as important as the performance

implications because it is the only structural member connecting the leading components (nose, supports, front shaft of runner hub etc.) with the trailing components (nacelle, rear supports, fixture/mooring supports).
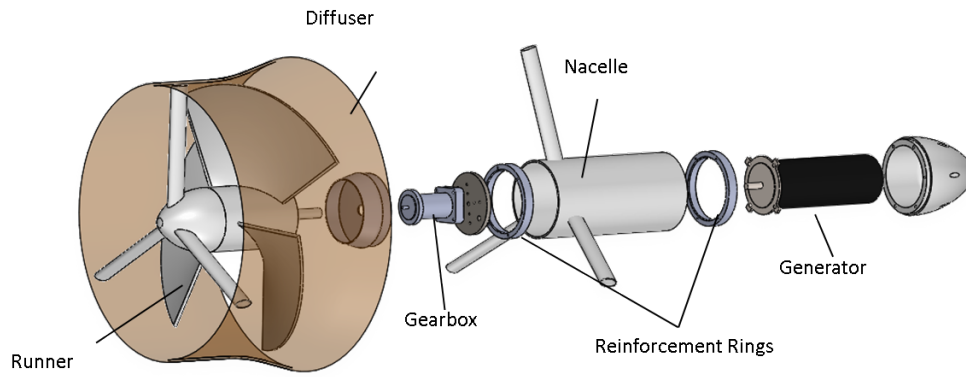
Figure 1: Exploded view of hydeokinetic turbine assembly [3]

The diffuser is the key design component for the entire system due to the performance and structural implications of the diffuser design combined with the difficulty of manufacture.

The nacelle contributes to a large portion of the surface area of the system while both housing the gearbox/generator and acting as the main support member of the system. Thus, although simple in design, it is of chief concern for analyzing the flow through the system. The gearbox and generator specifications are determined by the numerical results and theoretical torque estimations.

Objectives and Outline of Thesis Work

The four chapters of this Thesis aim to explain methods used to produce a functional prototype that produced the predicted results in [3, 4]. Chapter 1 provides an overview to the general hydrokinetic theory applied to the design of the prototype.

Chapter 2 consists of a brief explanation of the numerical methods and optimization techniques used with the design specifications to determine a runner and diffuser geometry. In Chapter 3, each critical component is analyzed and the design of each is refocused on manufacturability. The comparative advantages and disadvantages of each method are also detailed relating to cost, prototype assembly, and scalability. Finding an economical approach is of chief concern to the research of this particular micro-hydrokinetic turbine and is as valuable as the results obtained by the prototype. The impact of each method on the performance of the turbine is analyzed in Chapter 4 while Chapter 5 explains the testing procedure in detail along with the conclusive results obtained in the final experiment.

Chapter 2: Numerical Methods and Theory

Reynolds Averaged Navier-Stokes Flow Model

The hydrokinetic device investigated operates in the presence of turbulence effects present within the flow field as well as those resulting from operation. Therefore, in order to accurately tabulate the both forms of turbulence in the turbine, an appropriate model must be implemented. The following highlights the derivations to allow for effective, efficient modeling of the unit in three dimensions.

The Reynolds Averaged Navier-Stokes (RANS) equation derived in this chapter is for the relative, rotational reference frame. The relative frame relates to the rotation speed applied to the turbine blade. Through this extension of the RANS equation, three dimensional simulations may be conducted using steady state analysis with the rotational frame. Each equation was formulated assuming incompressible flow. Reynolds

decomposition is used to separate velocity components of the Navier-Stokes equation

into two separate components: a time-averaged term denoted by U and a fluctuation term

denoted by u'. The velocity term and the time-average term are as follows:

$$u_i(x_i, t) = U_i(x_i) + u'(x_i, t) \tag{1}$$

$$U_i(x_i, t) = \frac{1}{\Delta t} \int_t^{t+\Delta t} u_i(x, t)dt \,, \Delta t_1 \ll \Delta t \ll \Delta t_2 \tag{2}$$

where $u_i(x_i, t)$ is the velocity term variable in both time and space, Δt is the time scale

over which the time-averaging occurs, and the terms Δt_2 and Δt_1 are the upper and lower

bounds of the time scale used for averaging. [5].

Rotational Reference Frame

Solving the equations for the rotational rotor in the absolute reference frame

becomes increasingly difficult. Therefore, the steady, non-inertial frame of reference is

used. The inclusion of centrifugal and Coriolis forces is necessary to transform the

transport equations from inertial to non-inertial reference frames. The conservation of

mass and momentum in the non-inertial frame of reference are listed below:

$$\frac{\partial w_i}{\partial x_i} = 0 \tag{3}$$

$$\frac{\partial w_i}{\partial t} + w_j \frac{\partial w_i}{\partial x_j} = -\frac{1}{\rho} \frac{\partial p}{\partial x_i} - 2\epsilon_{ikl}\Omega_k w_l - \epsilon_{ikl}\epsilon_{lst}\Omega_k \Omega_s x_t + v \frac{\partial^2 w_i}{\partial x_j \partial x_j} \tag{4}$$

In equations (3) and (4), relative velocity w, permutation symbol ϵ and angular velocity

of the reference frame Ω are represented.

$$\frac{\partial W_i}{\partial x_i} = 0 \tag{5}$$

$$\frac{\partial W_i}{\partial t} + \frac{\partial (W_i W_j)}{\partial x_j} + \frac{\partial (\overline{w_i' w_j'})}{\partial x_j}$$

$$= -\frac{1}{\rho}\frac{\partial P}{\partial x_i} - 2\epsilon_{ikl}\Omega_k W_l - \epsilon_{ikl}\epsilon_{lst}\Omega_k \Omega_s x_t + \nu \frac{\partial^2 W_i}{\partial x_j \partial x_j} \qquad (6)$$

where W is the time averaged relative velocity and the $\overline{w_i' w_j'}$ is the time averaged

fluctuation term.

Turbulence Modeling

The time averaged fluctuation transfer term $-\overline{u_i' u_j'}$ introduces six unknowns,

creating an open system. Turbulence modeling is used to derive relations for the six

unknowns and solve the system of equations.

The Boussinesq eddy-viscosity approximation [6] can be used to generate

additional relationships. Assuming a linear relationship between the stress and strain

within the flow, the specific Reynolds stress tensor and mean strain-rate tensor are

determined. To define the Reynolds stresses:

$$k = \frac{1}{2}\overline{u_i' u_j'} \qquad (7)$$

$$\tau_{ij} = \frac{2}{3}k\delta_{ij} - \nu_T \left(\frac{\partial u_i}{\partial x_j} + \frac{\partial u_j}{\partial u_i}\right) \qquad (8)$$

where k is the turbulent kinetic energy, δ_{ij} is the Kronecker delta, and ν_T is the kinetic

eddy-viscosity. Introducing two dissipation terms:

$$\varepsilon = c_D k^{3/2}/l = \beta^* \omega k \qquad (9)$$

where c_D and β^* are closure coefficients, l is the turbulence length scale, ε is the

turbulent dissipation rate, and ω is the specific turbulent dissipation rate. The k-ω Shear

Stress Transport (k-ω SST) developed by Menter [7, 8] is a turbulence model based on

the Boussinesq eddy-viscosity approximation. The equations for kinematic eddy

viscosity, turbulent kinetic energy, and specific dissipation rate are included below:

$$\nu_T = \frac{\alpha_1 k}{\max(\alpha_1 \omega, SF_2)} \tag{10}$$

$$\frac{\partial k}{\partial t} + U_j \frac{\partial k}{\partial x_j} = \tau_{ij} \frac{\partial U_i}{\partial x_j} - \beta^* k\omega + \frac{\partial}{\partial x_j}\left[(\nu + \sigma_k \nu_T)\frac{\partial k}{\partial x_j}\right] \tag{11}$$

$$\frac{\partial \omega}{\partial t} + U_j \frac{\partial \omega}{\partial x_j} = \alpha S^2 - \beta \omega^2 + \frac{\partial}{\partial x_j}\left[(\nu + \sigma_\omega \nu_T)\frac{\partial \omega}{\partial x_j}\right]$$

$$+ 2(1 - F_1)\sigma_{\omega 2} \frac{1}{\omega}\frac{\partial k}{\partial x_i}\frac{\partial \omega}{\partial x_i} \tag{12}$$

where ν_T is the turbulent eddy viscosity, ν is the kinematic viscosity, k is the turbulent

kinetic energy, ω is the specific dissipation rate, α_1 is a closure coefficient, β is a closure

coefficient, S is the mean rate-of-strain tensor, and F_1 and F_2 are blending functions. The

blending functions of the original SST model are not included amongst equations (10)

through (12). The blending functions, closure coefficient values, and derivations may be

obtained from Wilcox [5].

Numerical Method

The finite volume method and the finite difference method are utilized in the

numerical methods to follow. In finite differencing, the partial differential equations are

discretized. In the finite volume approach, the integral form of the equation is discretized.

Finite volume discretization is increasingly advantageous with increasing complexity of

the target geometry. The finite volume discretization utilizes control volumes.

The fundamental basis of the finite volume method is the control volume integration with Gauss' divergence theorem. The divergence theorem states that the net flow is equal to the sum of all source terms minus the sum of all sink terms.

$$\iiint_V (\nabla \cdot \vec{F})\, dV = \oiint_S (\vec{F} \cdot \vec{n})\, dS \tag{13}$$

where V is volume, S is surface, $\vec{F}$ is a vector field, and $\vec{n}$ is the outward pointing unit normal vector. Applying equation (13) to generic flow variable, ϕ, in the x-direction, the change of variable ϕ in the x-direction can be approximated as:

$$\frac{\partial \phi}{\partial x} = \frac{1}{\Delta \forall} \iiint_\forall \frac{\partial \phi}{\partial x} d\forall = \frac{1}{\Delta \forall} \iint_S \phi dA_x \approx \frac{1}{\Delta \forall} \sum_{i=1}^{N} \phi_i A_{i,x} \tag{14}$$

where $\forall$ is the discretized volume, $A_{i,x}$ is the x-direction projection of the *i*th face of the discretized volume, and N is the number of closed surfaces existing on the discretized volume. Equation (14) provides the fundamental basis for solving partial differential equations of flow variables in three-dimensional geometry.

Finite Volume Methods Implemented

Coupled [9] pressure-velocity solvers were implemented to obtain the steady state predictions of flow field conditions and performance characteristics of the turbine unit. Skewness corrections were also applied to account for cells to reduce convergence difficulties present where cells may experience distortion resulting in issues with mass flux values between adjacent cell faces. In steady-state simulations a Coupled solver was used to determine the resulting flow field. The Coupled algorithm is more accurate than Semi-Implicit Method for Pressure Linked Equations (SIMPLE) solvers for steady-state

simulations. It also is more efficient when solving the continuity and momentum equations in single-phase simulations.

Boundary Conditions

Simulations were comprised of a rectilinear or semi-cylindrical channel comprised of two separate subdomains. The first region represented the river domain and turbine domain. Figure 2 includes the isometric view of the two-domain setup, along with the cross sectional view and an example turbine geometry.
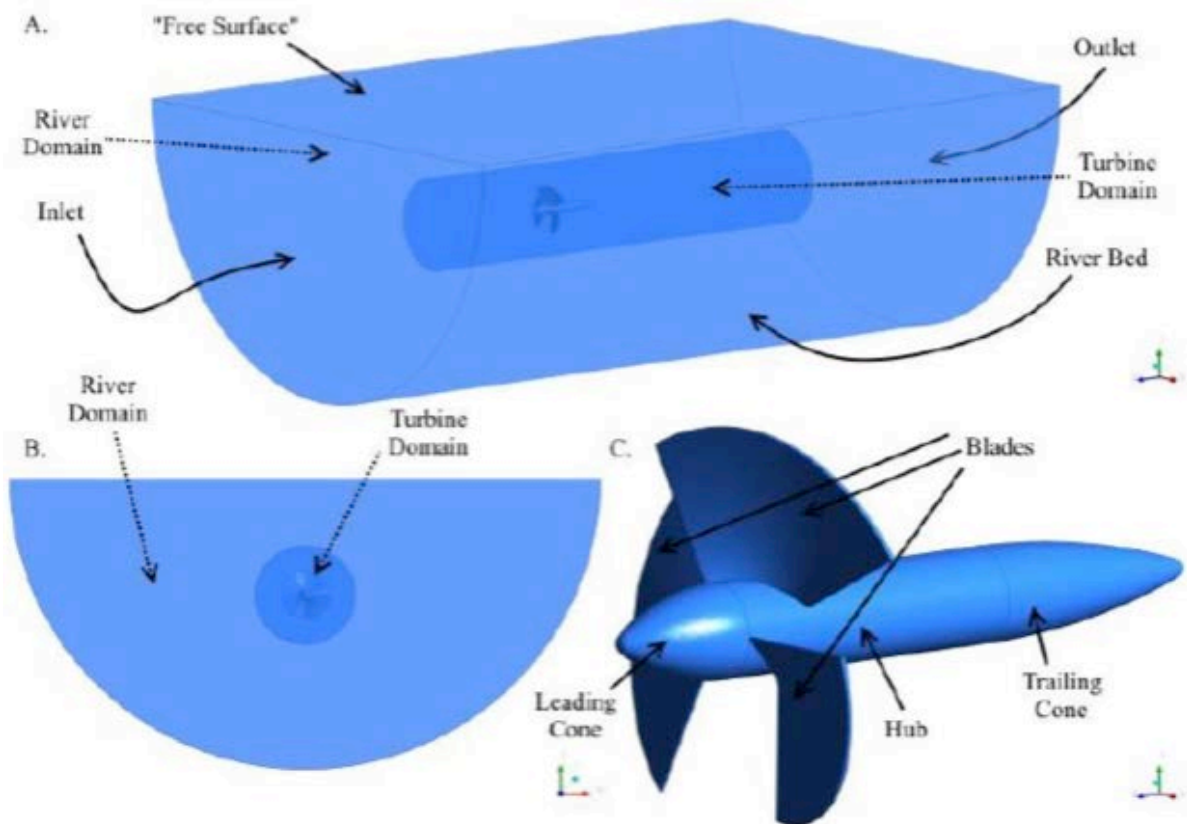

Figure 2. General boundary condition setup for RANS-CFD analysis [10].

For single phase, steady state analysis, the turbine domain from Velocity was specified at the inlet and a zero pressure gradient, constant gauge pressure condition was applied at the outlet. No slip boundary conditions were applied to the turbine rotor and

the river bed. The turbulent boundary conditions at the inlet and outlet were specified

using the following:

$$I = 0.16\left(Re_{D_H}\right)^{-1/8} \tag{15}$$

$$l = 0.07D_H = 0.07\left(\frac{4A}{P_w}\right) \tag{16}$$

Where I is turbulent intensity, D_H is hydraulic diameter, Re_{D_H} is the Reynolds number

based on the hydraulic diameter, and P_w is the wetted perimeter of the channel.

TurboGrid

TurboGrid was used to formulate the grid structure about the blade surface, the

hub, and the outer shroud of the blade tip. This is of particular advantageous in areas

where turbulence and adverse pressure gradients are more likely to exist. The ability to

control the grid size and structure facilitates capturing the boundary layer and flow

separation. Figure 3 and Figure 4 shows an example of the mesh produced in an axial

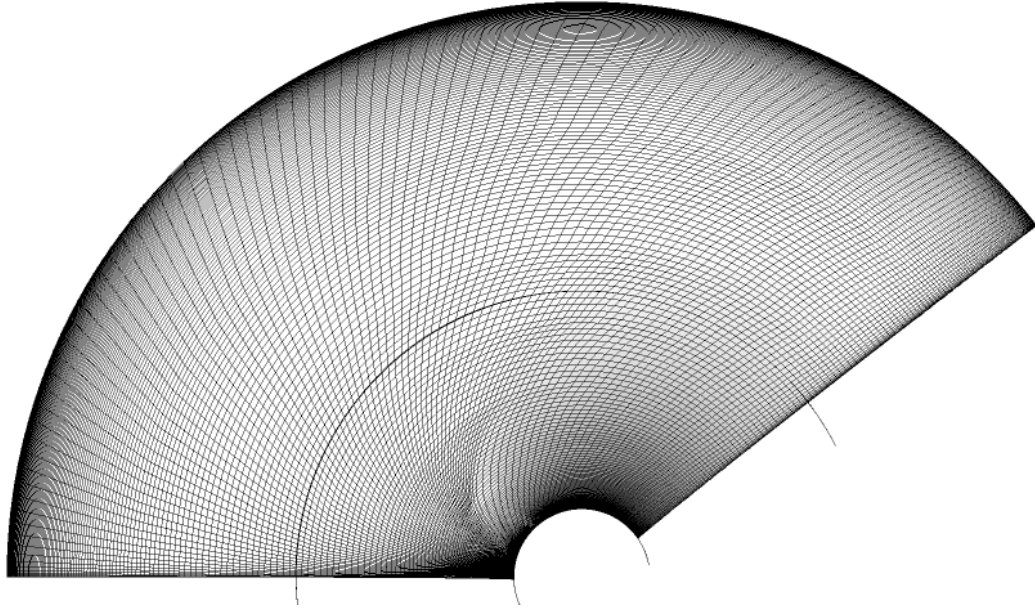view and the inflation layer along the hub and outward away from the blade.

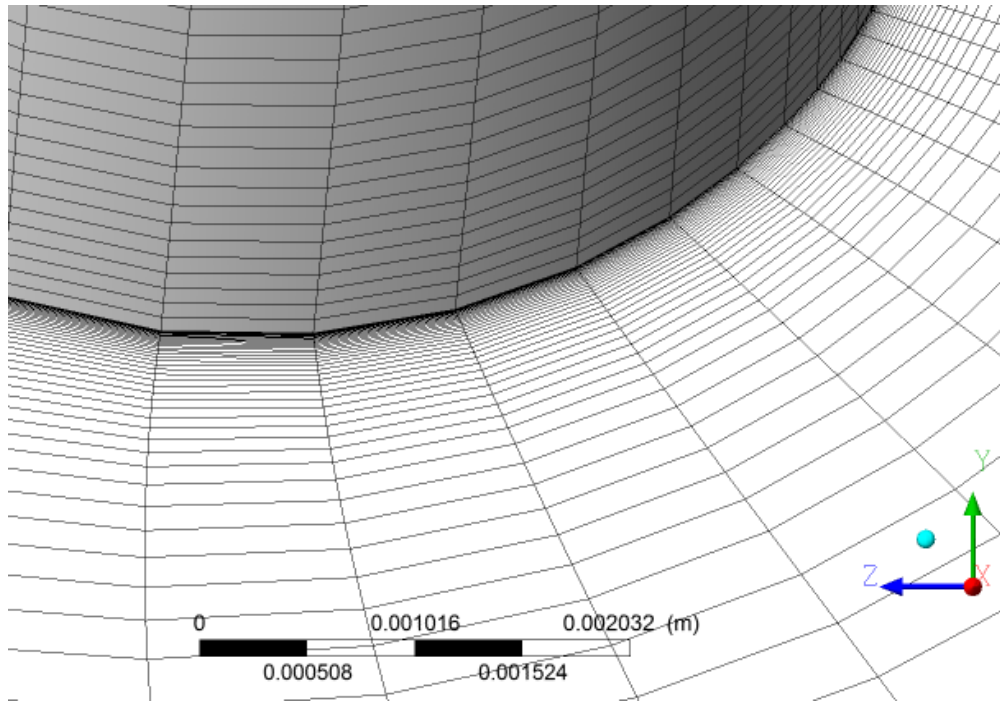Figure 3. Turbine domain axial grid structure [3]

Figure 4. Boundary layer inflation along the blade and hub [3]

Chapter 3: Design Considerations

Motivation

While the numerical methods used in [11, 12, 4, 3] contribute greatly to the theoretical implications of the design, the exact geometry is not easily reproducible for a physical experiment. The design was revisited in order to facilitate the production of a functioning full scale prototype while mitigating the effects on performance relative to the ideal optimized geometry of both the blade and the diffuser.

A major design consideration for this prototype was structural integrity. Preventing any mode of structural failure was imperative due the testing conditions. The prototype was tested in the CWC at David Taylor Model Basin where a structural failure could cause costly or irreparable damage. With axial thrust calculations for individual components readily available from [12, 3], worst-case estimations can be made on most of the critical design components. Structural rigidity must also be considered. A rotational imbalance in the blade or vibration of the system under load during flow conditions could also cause failure.

A minor design specification driving the design of each component was a requirement that no one component weighed more than 80lbs. This specification theoretically allows each component to be carried by a team member responsible for deploying the system. In the next phase of design, each component would be further optimized for portability, encompassing ease of transportation and ability to pack and hold on to individual components.

Runner

The final blade geometry was optimized by Scheicher *et al.* [10] using the rapid CFD processes that were reviewed in Chapter 2. The geometry optimized for a flow speed of 1.5m/s, a flow rate determined to be the average of the most accessible sites within the performance criteria from available river data [2]. There are two parameters critical to the successful manufacture of the runner; the tolerance stack up on blade assembly and the strength of the shaft.

The tolerance stack up on the blades needs to be considered to ensure a radially symmetric part. The center of mass must be as close as possible to the central axis of the runner to avoid a rotational imbalance. The tolerance is determined by the manufacturing process. The blades will be made separately and welded to the central hub. The hub was turned down from solid bulk aluminum. Standard turning operations above 6.0in in diameter have a diametrical tolerance of +/-0.003in and +/-0.001in on operations below 6.0in diameter[machinery's]. The blades were machined on a 4 axis machine that can achieve a tolerance of +/-0.005in on the complex surfaces of the blade. Assuming worst-case conditions for the turning operation, the hub can be a maximum of 0.0015 off center. At optimal blade rotation speed of 115 rpm, the maximum imbalance for caused by the hub is negligible (0.145N). Since the hub accounts for 70% of the mass and the symmetry of the three blades offsets any major imbalances due to the distance of the center of mass of the blade from the center axis of rotation, the tolerance on the blades would need to be many magnitudes higher than that of the hub. This is not the case. Thus, a force caused by an imbalance due to tolerance stack up is negligible.

More analysis is needed to analyze the stress and deflection of the blades when in operation at ideal conditions.
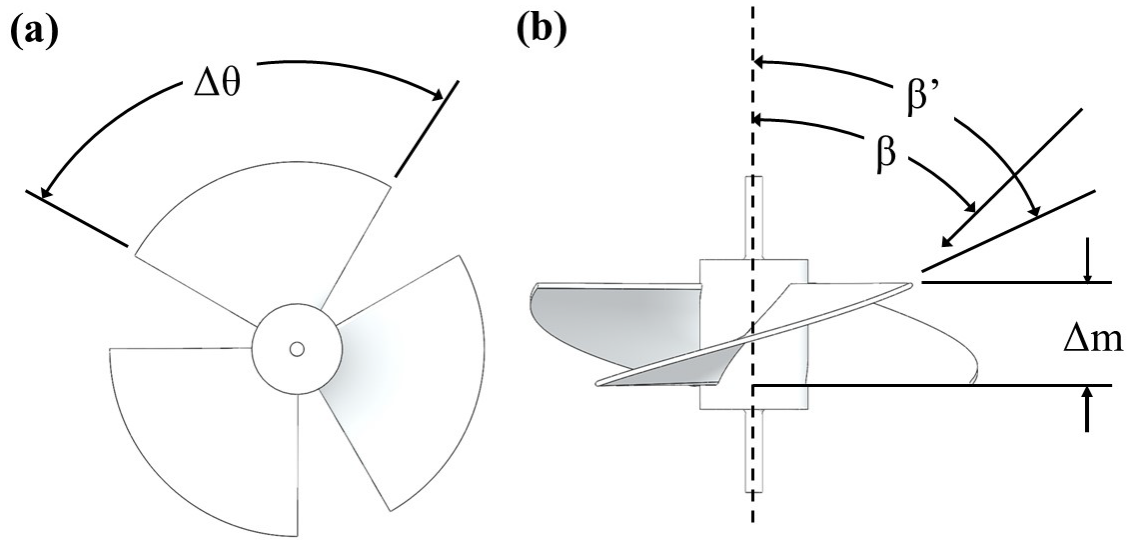

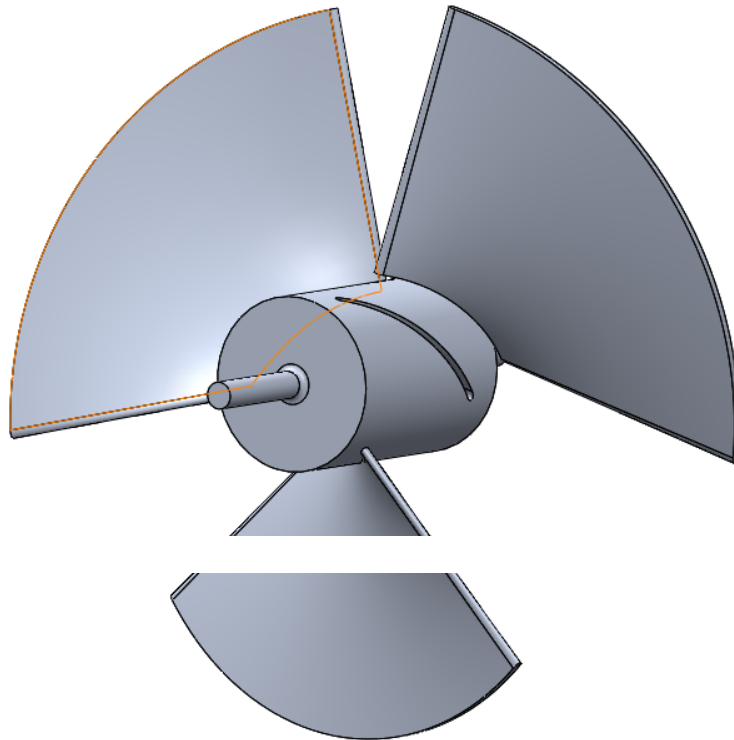Figure 5. Blade design (a) front view and (b) top view [12].

Figure 6: Assembly of runner

Diffuser

The diffuser is the key component to the system's performance and structural integrity. The design of the diffuser was chosen from [4] and optimized for 1.5 m/s flow conditions. There are three parameters that control the performance of the diffuser; area ratio, length, and flange length. As shown in Table 1, the power production is not sensitive to the flange length, meaning it is not an essential component of the design in the diffuser. The performance response of the initial optimization of the diffuser is shown in Figure 7.The optimization output for maximum power is shown in Table 2 [3]. The angle is a direct representation of the area ratio of the inlet and outlet of the turbine. Both the power and diffuser thrust are significantly affected by the area ratio. Therefore, maintaining the area ratio is of chief importance when fabricating the diffuser.
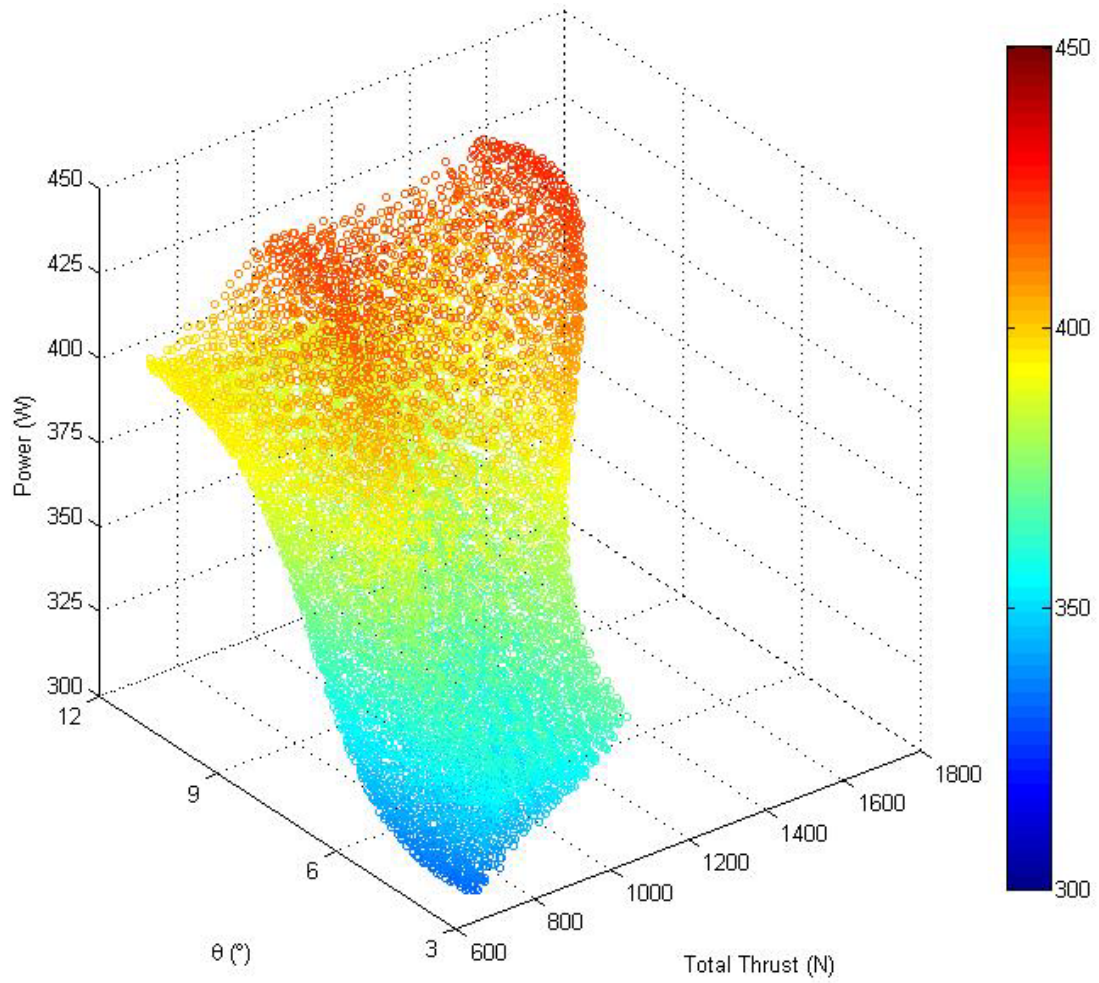
Figure 7:Performance response for diffuser optimation (2m/s) [4]

Table 1: Sensitivity at Peak Performance [13]
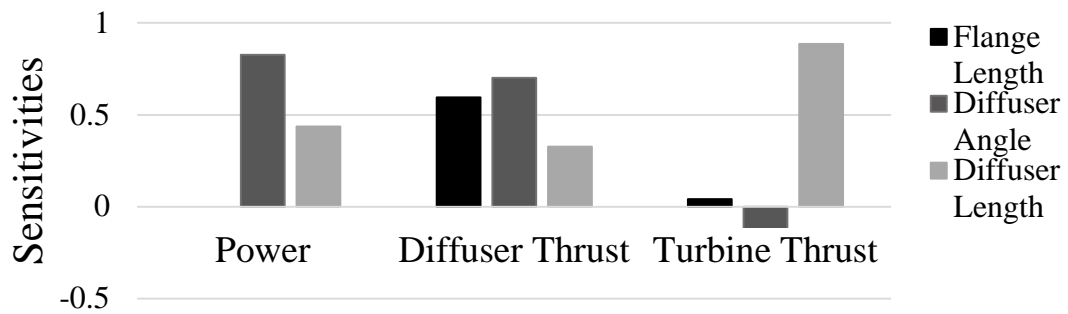
Table 2: Peak Performance Parameters [13]

Parameters	Maximum Power		
T (m)	0.0789	0.0846	0.0247
θ (°)	10.4	10.8	9.6
L (m)	0.912	0.839	0.771
Power (W)	425.0	422.9	418.4
Thrust Diffuser (N)	1221.0	1281.6	590.8
Thrust Turbine (N)	344.2	341.6	334.5

The initial optimizations on the diffuser were a conical geometry. The optimal area ratio was chosen in [14, 3], then a curve was added to better maintain the desired flow properties through the majority of the meridional length while providing a smooth transition to the increased outlet diameter. While this geometry proved to be effective in the CFD simulations, the difficulty of fabrication was greatly increased. To lower cost and time frame of manufacture, the design was altered.

Figure 8: Optimized diffuser geometry [4]

The objective of the alteration was to drastically facilitate the fabrication of the diffuser while mitigating potential power losses. It was shown in the CFD simulations

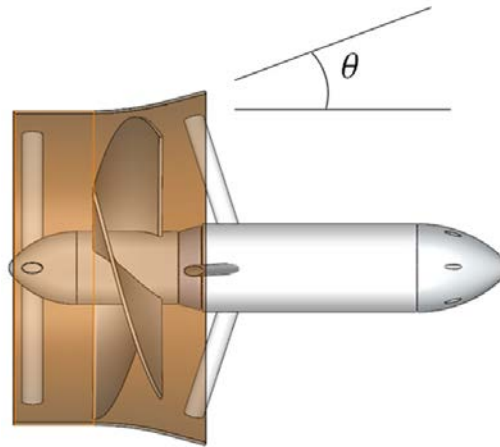that the smoothness of the curve did not heavily influence the power production. The change in design is represented in Figure 8 and 9.
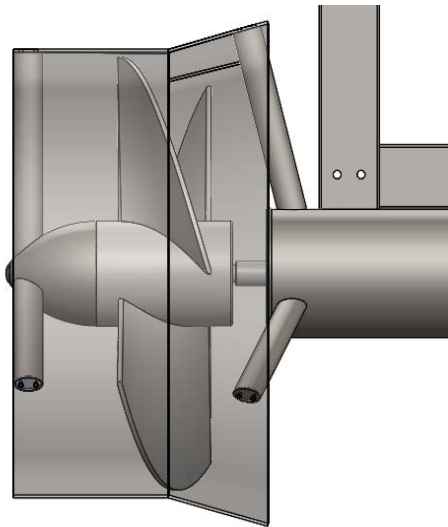
Figure 9: Redesigned diffuser geometry to facilitate manufacture

This minor change had negligible effects on the performance of the prototype while significantly increase the manufacturability. The two components of the diffuser were fabricated with precise rolling operations and seam welded along the circumference of their joining edges. To assure that the diffuser was structurally stable, 304 stainless steel plate with a thickness of 0.313" was chosen. This thickness is important as the strength and thickness of this material are critical parameters in rolling operations. The flat blank of the detail is shown in Figure 10. The conical portion of the diffuser was fabricated by controlling the feed direction. The feed direction must remain tangent to the perimeter of the crescent shaped flat pattern. The tolerance on the diffuser is very critical to the functionality of the entire system. The front and back supports provide locating features for the runner assembly. The alignment of the central axis is important for reducing vibration and providing a sufficient seal between the shaft of the runner and the

nacelle housing the electrical components. The tolerance achieved on both the cylindrical and conical portion of the diffuser were specified at +/-0.005. This is tight enough to ensure a clean assembly, well within the performance of the rolling operations with multiple passes, and a negligible misalignment over the length of the runner assembly between leading and trailing components.
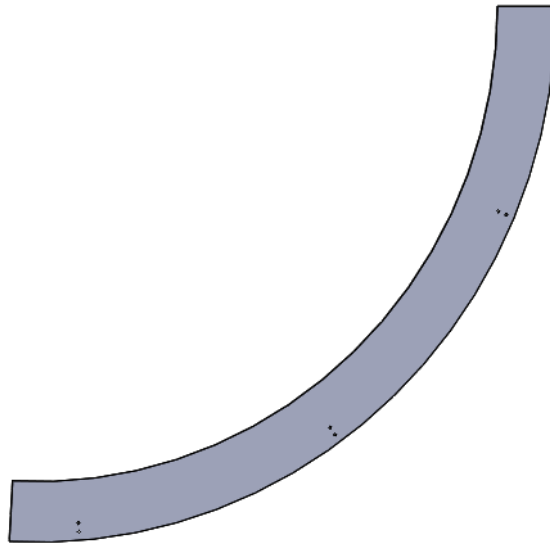
Figure 10: Flat pattern of conical diffuser component, designed for rolling operation

Nacelle and Elliptical Supports

The nacelle and supports are key structural components to the system. The supports provide the only connection between the runner, diffuser and the rest of the assembly. The supports are chiefly responsible for axial stability at optimum flow conditions. Although an individual support is unlikely to cause critical failure, the rigidity provided by the combination of supports was critical to the successful results of the prototype. The elliptical cross section was chosen to both reduce drag and increase

22

bending resistance from axial loading. A tube of elliptical cross section, 14ga 304 stainless steel was used, shown in Figure 11.
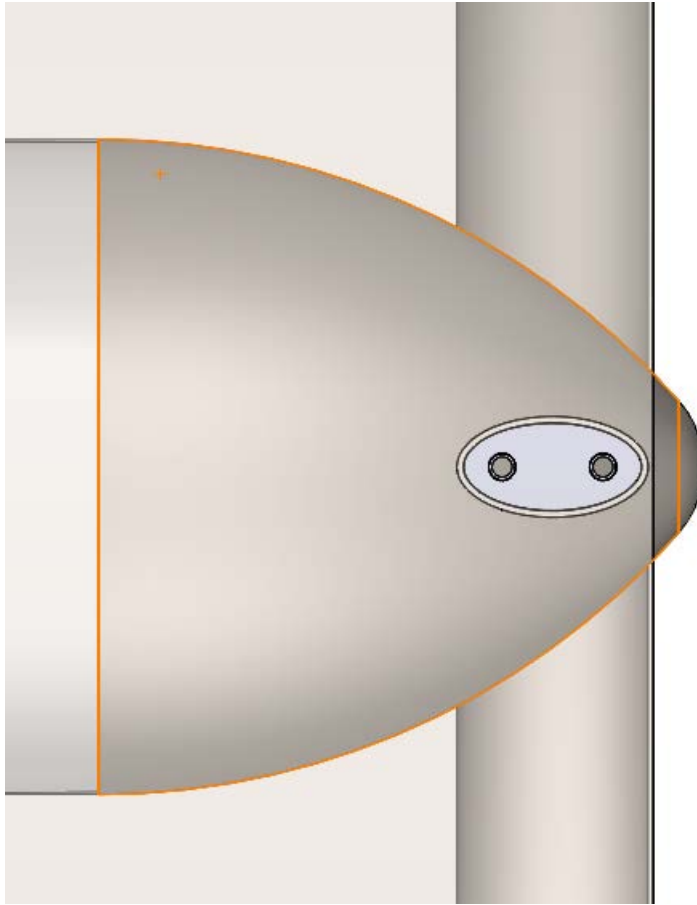
Figure 11: Cross section of elliptical tube, 2" and 1" major and minor axis, respectively

The distributed load on each support can be estimated using worst-case assumptions. $|U|$ is calculated using the tip speed of the blade:

$$|U| = \sqrt{U_\infty{}^2 + \left(\frac{\omega D}{2}\right)^2} \tag{1}$$

Using equation (1) to determine the distributed load, a comparison can be made between the circular ($C_D = 1.17$) and elliptical cross section ($C_D = 0.4$) using the Moody Diagram. The distributed load on the circular and elliptical supports was estimated to be

198.55N and 67.88N, respectively. Both loads are negligible when considering the structural strength of tube, but have a differing impact on the thrust associated with the system.

The elliptical supports were purchased as a tube extrusion. The tolerance along the axis of the tube is +/-0.010in, however this is not critical to the design. Each tube end was then machined in a 5 axis CNC mill (tolerance of +/-0.005in) to create the necessary radius and angled cuts for a secure fit to the diffuser, leading cone, and body of the nacelle. The supports, when secured to the diffuser during assembly, provide the only locating features for both the leading nose and the nacelle. The tolerance stack up of the diffuser and support combine for a worst-case fit of +/-0.010in. This was combated on the leading nose by extending the length of the supports by 0.005in and machining a slot of 0.015in slots in the leading nose. This would provide enough room to align the assembly before welding without creating weld gaps, decreasing the instances of potential critical failure points. The supports leading to the nacelle were offset from the surface of the nacelle by 0.010in. This ensured that the alignment of the nacelle could be compensated in all directions when assembling the shaft seal, nacelle front cap, gearbox, and generator. With these components installed, the trailing supports could be secured to the diffuser then welded to the nacelle. Each support was marked with a corresponding location on the diffuser to ensure the fit was maintained through various reinstallations throughout the prototyping process.

The nacelle is also responsible for absorbing the torque of the runner assembly. The torque generated by the runner must be transfer through a gearbox to a generator, which is to remain fixed within the nacelle.
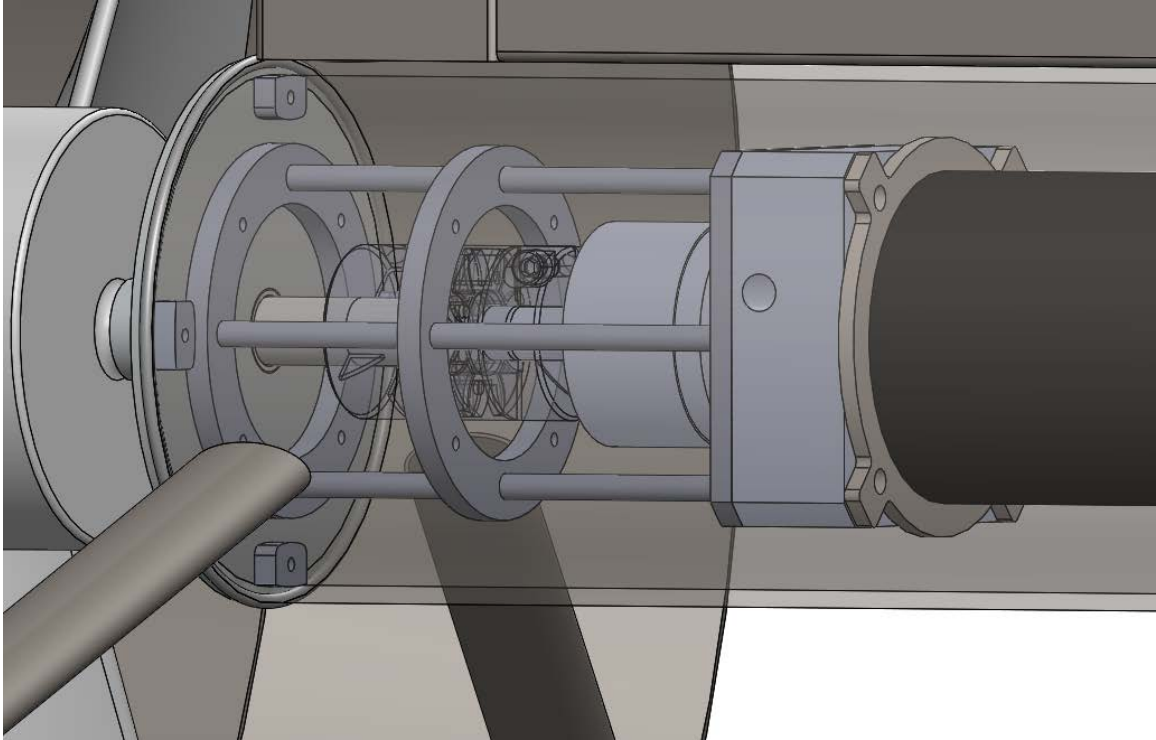
Figure 12: Providing a structure to fix the generator within the nacelle

This was achieved through the use of stabilizing rings and rods running the length of the gearbox. The torque predicted in [12] was estimated to be 32Nm. This torque will be realized by the structure comprised of the rings and rods connected to the faceplate of the generator and gearbox. The rings are 0.5in plain carbon steel and the rods are 0.375in diameter plain carbon steel. A cross section of the set up is shown in Figure 13. With an estimated torque of 32Nm, each shaft experiences a load of 31.47 lbs. Without the central ring shown in Figure 12, this would translate to an angle of twist along the length of the gearbox equal to 6.4 degrees. With the central ring, the angle of twist along the length of the gearbox is reduced to 0.5 degrees, an order of magnitude smaller than the structure without the additional stabilizing ring. This torque is transferred to the front face plate of the nacelle, to the tabs welded to the inside on the nacelle, to the fixture assembly which

is fixed to a point above the surface of the water. Therefore the nacelle is both responsible for keeping the generator fixed relative to the rotation of the blade as well keeping the assembly axially aligned with the flow throughout testing. The fixture is discussed in greater detail in Chapter 4.
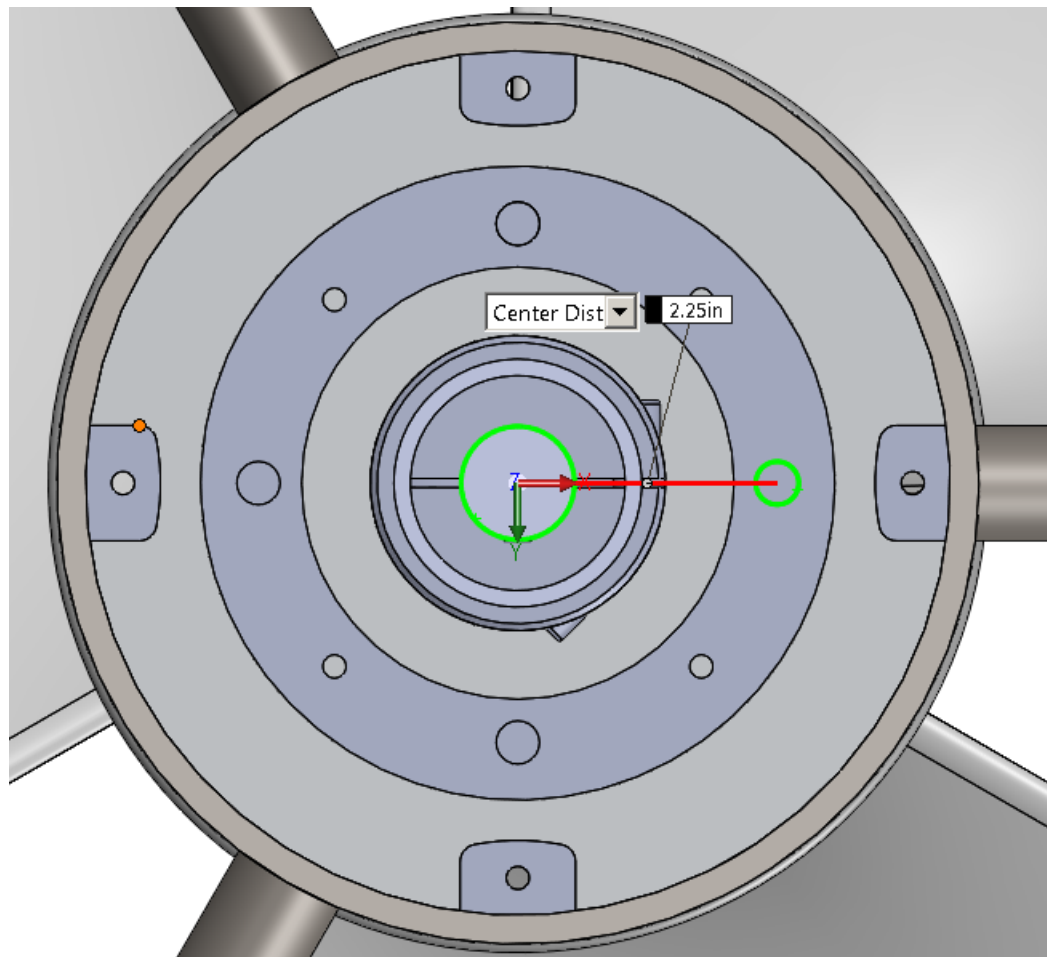
Figure 13: Axial Ring Structure Cross Section

The trailing cap of the nacelle was originally designed and simulated as a tapered cone to reduce thrust generated by the nacelle geometry. The cost savings of replacing the tapered cone with a disk cap far outweighed the reduced thrust due to the tapered

trailing cone. The estimated increase in thrust was determined negligible when comparing the anticipate results of the simulations and the final results obtained in full scale testing.

Generator and Gearbox Selection

According to the optimization data obtained by Schleicher [12, 3], the estimated power generated by the turbine was 431.4 W of mechanical power at 1.5m/s. The generator selected for the prototype was a 10 A, continuous DC permanent magnet generator made by Windstream LLC. At 48V, the generator was capable of producing between 250 and 1000 watts continuously without causing permanent damage to the generator. According to the optimization data, the shaft rotation speed at 1.5m/s will be 115rpm. To hit our target power production with the generator, a gear ratio of 10:1 was used to produce an input shaft speed of 1150 rpm, corresponding to just over 400 W.
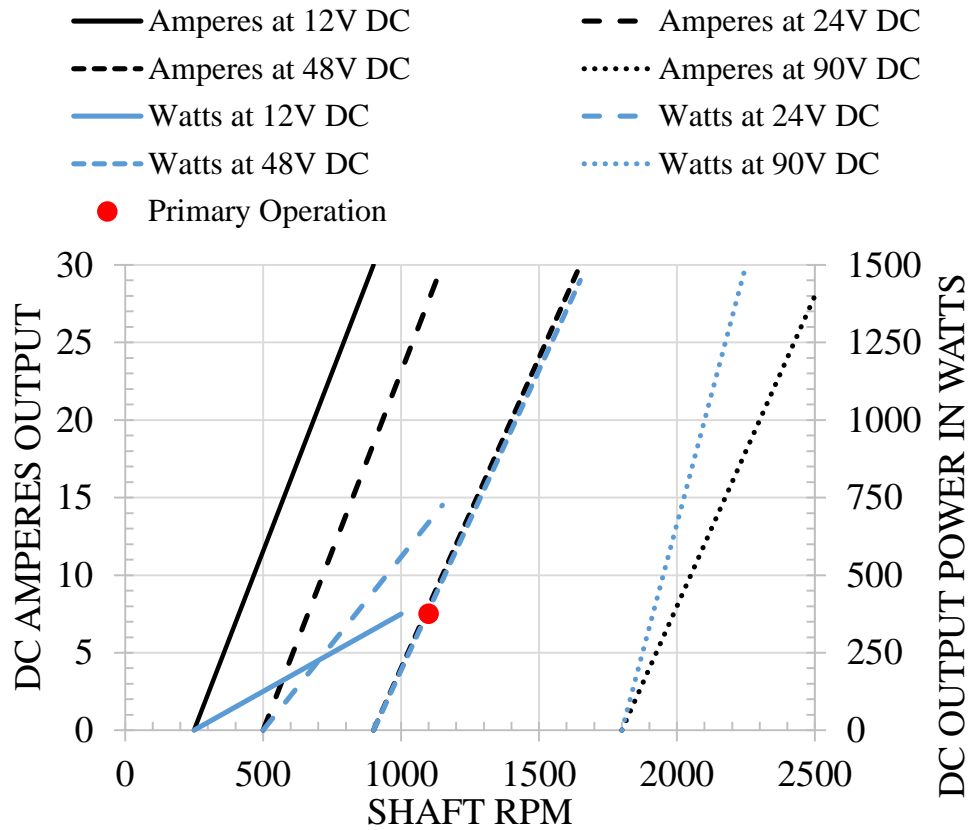
Figure 14: RPM vs DC AmpsOutput [3]

Chapter 4: Prototype Assembly and Test Prep

Prototyping and Mooring

The process of assembling the prototype had significant design implications on

the turbine. For example, the design of the internal support structure for the generator and

gearbox assembly had to be installed after runner assembly, shaft seals, bearings and

front plate of the nacelle. Considerations mentioned earlier about the alignment of the

shaft axis with the gearbox and generator were realized during the assembly of the

diffuser, supports, and nacelle. The alignment was maintained through each weldment.

The mooring fixture was design in favor of stability compared to standard types of mooring such as chains or ropes. Mooring chains provide only enough resistance to fight the thrust generated by the turbine and do very little to aid in axial stability. For this reason, the solid beam fixture was designed. The assembly in Figure 15 shows the final design implemented for the full scale test.

Figure 15: Fixture assembly

The fixture assembly is comprised of two steel rectangular tubes welded in along the length of the nacelle, a 5.5ft beam, and a fixture plate used to fasten the prototype to a fixed m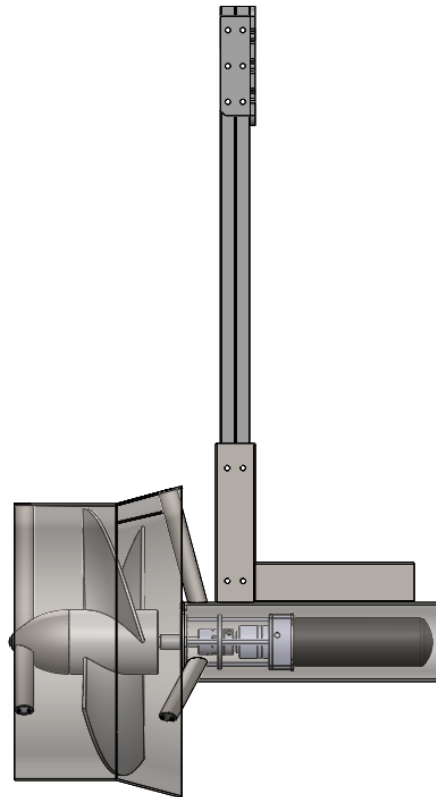ounting plate above the surface of the water. The rectangular tubes welded along the nacelle provide a very strong base for the beam. The beam is placed into the large

rectangular tube and fastened with 1/2in bolts. The tube is 4"x2" and 0.125" thick. The vertical portion was drilled out using a Bridgeport Mill. The horizontal and vertical tubes were then arc welded to the nacelle. Stainless steel filler wire of 0.035 inch diameter with an argon, helium, and C02 shielding gas mixture was used with constant voltage parameters. GMAW welding techniques were used on the connection between the trailing supports and nacelle. GTAW welding techniques were used by a certified welder on the trailing cap of the nacelle to ensure a water tight fit. A gasket was placed between the two flat surfaces prior to welding.

The fixture plate in Figure 16 is then fastened to the top of the beam. The two long brackets were waterjet cut from 0.5" plain carbon steel. Each plate had the bolt pattern shown on a Bridgeport mill and then fastened to the beam. The beam and bracket plates were placed on the mounting plate and clamped in position to be welded on the outside edges. The inside edges were not welded because the fillet created would cause interference when inserting the beam into the bracket for fastening.
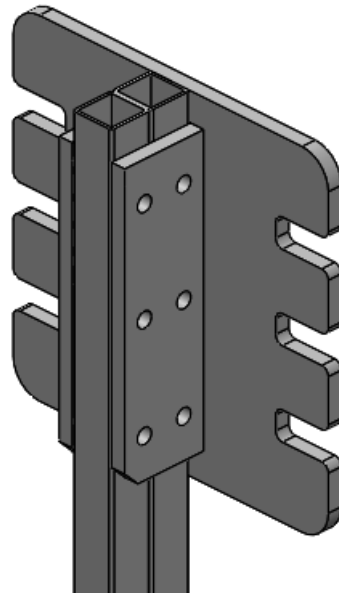
Figure 16: Mounting plate and bracket

The beam was composed of two 1.5" square 0.25in thick tubes welded together along the length of the tube. The ideal depth of the water channel testing was 4.5ft from the bottom of the fixture plate location above the surface. The beam was design to withstand the moment generated by the axial thrust produced by the generator. An estimated 224.3 lbs of thrust is generated at a flow speed of 1.5m/s. Using a cantilever beam equation and estimated moment of inertia of the beam, the total deflection is estimated to be only 0.32in. Yielding of the fixture occurs at a flow speed of 4.8m/s according to estimated thrust data.

The fixture plate and bolts must withstand a moment of 1009.4 ft lb about the bottom edge of the plate and shear load of 287 lbs, or the weight of the entire assembly. Worst-case scenario is 100% load on the bolt closest to the edge of the plate fixture shown in Figure 17.
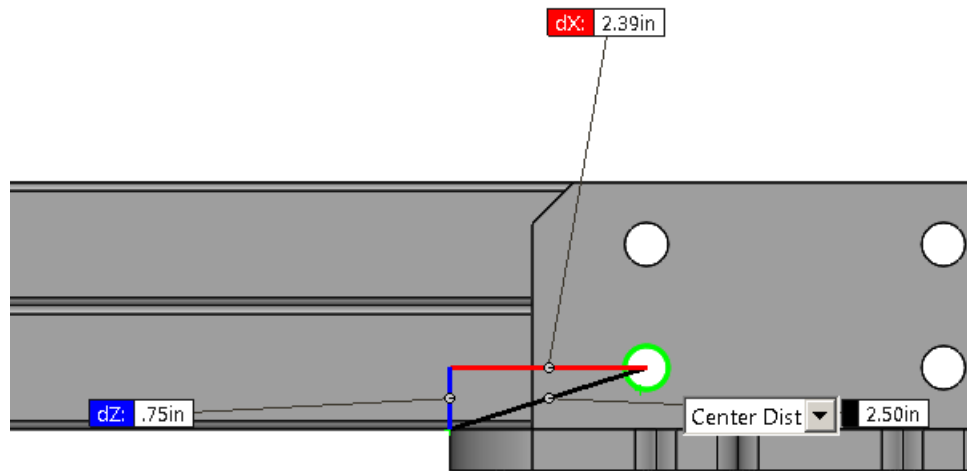
Figure 17: Worst-case single bolt scenario

Assuming only one bolt, the maximum shear force experience by this bolt is 4840
lbs and a shear stress of 24,700 psi. The 0.5" grade 8 bolts used are rated for shear
strength of 90,000 psi. Therefore, the worst-case scenario is not negligible but safe
nonetheless. The same worst-case scenario can be applied to both the bolts used to fix the
plate to the fixture above the surface and the fixture at the base of the nacelle. In the case
of the plate fixture, the six 7/8" grade 8 bolts are used to fix the plate to the mounting
plate of the bridge at the CWC. Since the bolts are the same in number, larger, and further
away from the center of rotation, it is reasonable to assume that the assembly is capable
of withstanding the load. For fixture at the lower portion of the beam connecting the
beam to the turbine assembly, the bolts experience far less force thus it is reasonable to
assume that the use of the same bolts will provide a stable fixture.

To prevent leakage into the nacelle, there are many locations that must be sealed appropriately. The shaft seal is the most critical of these. The shaft seal selected was double lipped spring loaded seal shown in Figure 13.
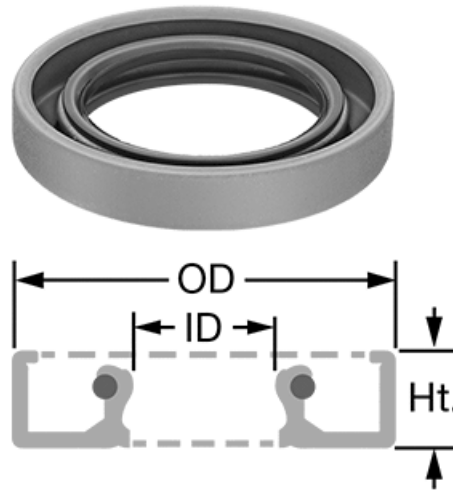
Figure 18: Shaft Seal

The seal is rated for a maximum pressure differential of 10psi for applications less than 1000rpm. The hydrostatic pressure due to depth is 2.3 psi. An enclosure was placed around the shaft seal. The tapered surface created between the blade hub and diameter of the nacelle by the enclosure diverts flow away from the shaft seal. Thus the dynamic pressure near the front face of the shaft seal is assumed to be negligible. Directly following the shaft seal is a needle bearing. The needle bearing was chosen because the addition axial length provides increased stability during rotation. It also carries the weight of the runner assembly via the trailing shaft. The leading shaft of the runner assembly is held in place by the leading nose and a solid composite bearing designed for submerged use. The cross section of the assembly components near the shaft seal, bearing, and coupling mechanism of the gearbox is shown in Figure 19.
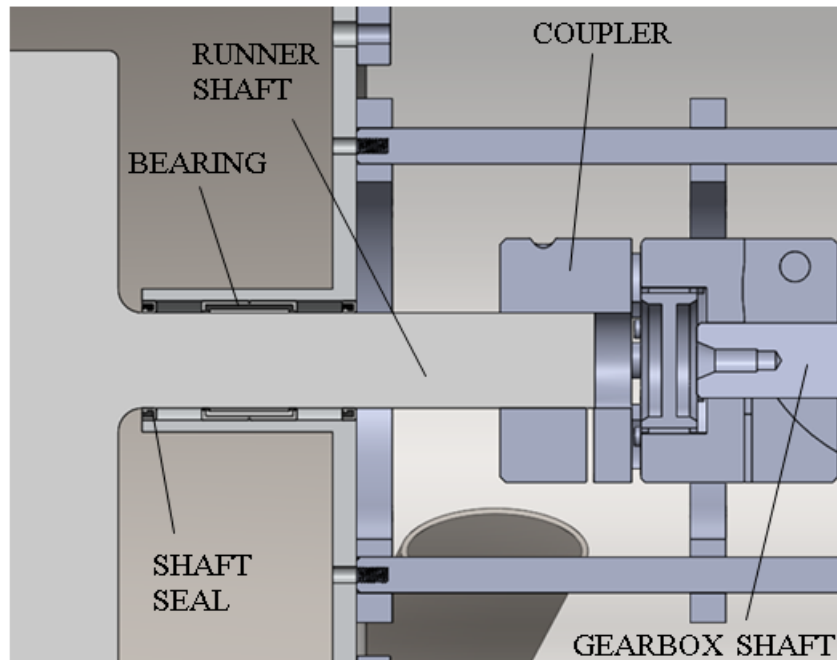
Figure 19: Cross section of shaft components

Other leakage points are shown in Figure 20. Location 1 was the last area sealed before testing because the nacelle is slid over the generator assembly and fastened to the nacelle's front face plate during the last step of assembly. Once sealed, the prototype cannot be disassembled without breaking this seal. The seal was created by chamfering the leading edge of the nacelle and trailing edge of the face plate to create more surface area for an o-ring and sealant. The sealant chosen was standard heavy duty RTV automotive sealant. It not only creates a water tight seal, but also remains mildly flexible to compensate for any minor vibrations or displacements that occur during testing.
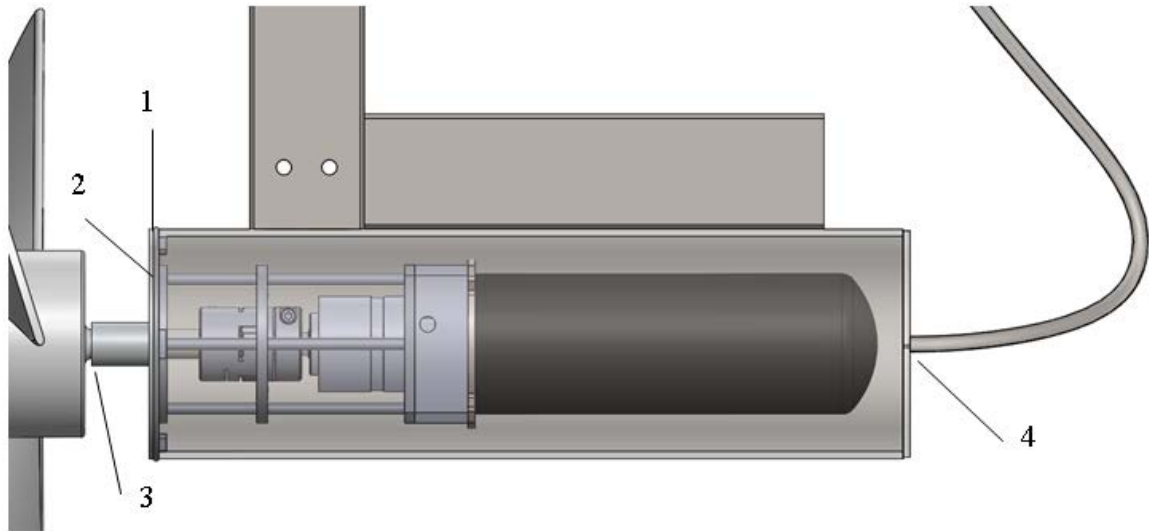
Figure 20: Critical sealing locations

Location 2 represents all of the screws and washers used to attached the generator

support components. All of these screws and washers were also sealed with the RTV

sealant as a precautionary measure. Location 4 represents and tube which accesses the

surface. This is used to carry the electrical wiring of the generator to the surface. A

sealing grommet, commonly used on composite boat hulls, designed for cable and hosing

was fastened and seal with RTV to the trailing face plate of the nacelle and coated with

RTV.

Chapter 5: Prototype Predictions and Performance

Initial Numerical Analysis

An approximation for the mechanical power produced by the turbine was determined to obtain torque estimations. These torque calculations were used in the selection of the generator. The results from characterizing the performance of these geometries are presented in Figure 23 and Figure 24. The power coefficient is presented in Figure 23 and thrust coefficient in Figure 24 as a function of tip-speed ratio. Results were obtained from the rapid CFD optimization process and therefore an error of 10% is expected. The final overall system efficiency is generated

$$C_{P,overall} = C_P \eta_{con} \eta_{gen} \eta_{gear} \tag{17}$$

Where η_{con} is the efficiency of the DC/DC converter, η_{gen} is the efficiency of the generator, and η_{gear} is the efficiency of the gear box.
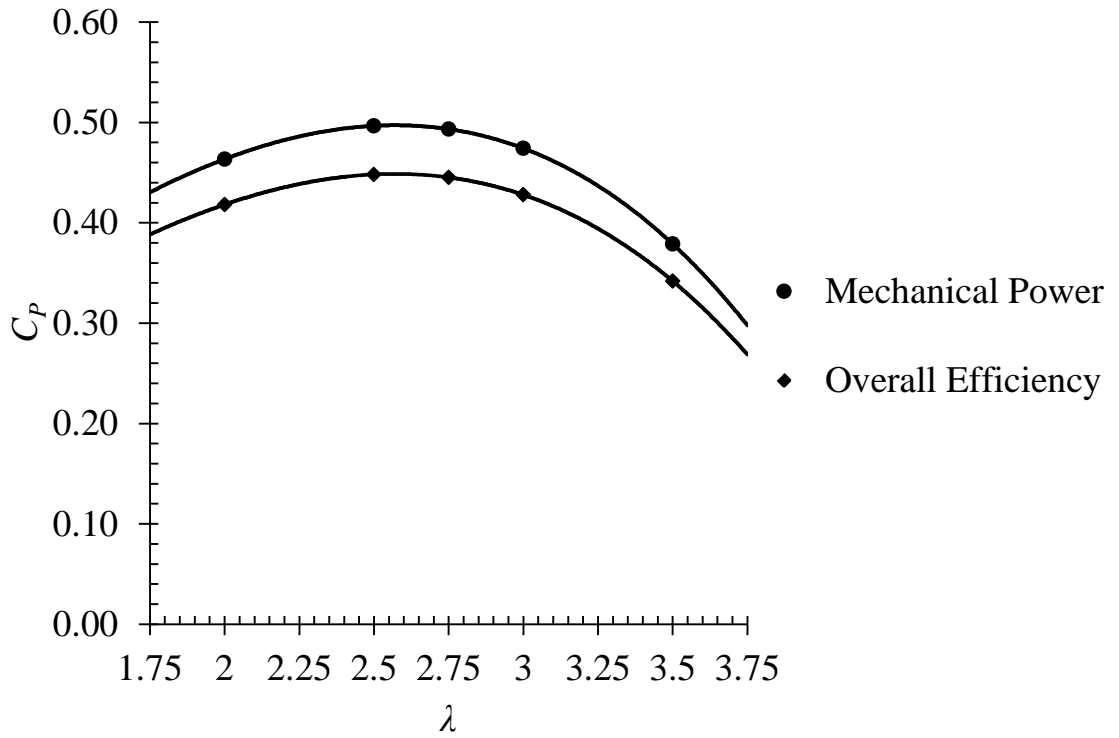
Figure 21. Prototype power coefficient predictions as a function of tip speed ratio [13]
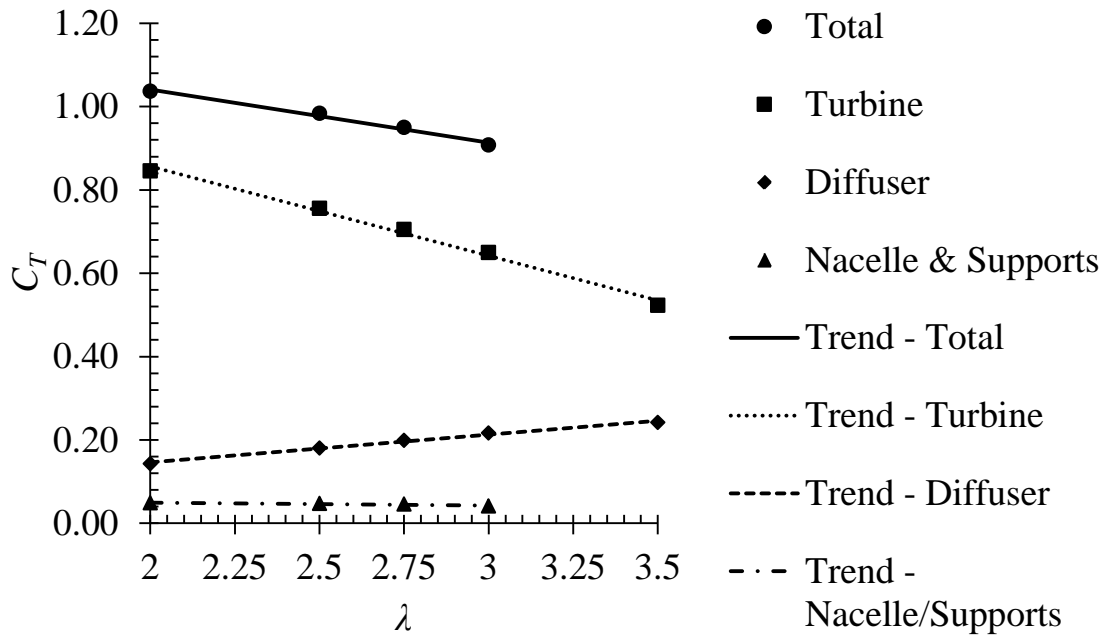
Figure 22. Prototype thrust coefficient predictions as a function of tip speed ratio [13]

Preliminary results of Schleicher's benchmark design [15] are shown. The results are obtained at a flow speed of 2.25 m/s. A 37.2% increase in power is realized with the inclusion of the diffuser. The results in Figure 23 only take into consideration the blade and diffuser geometries i.e. the leading cone, nacelle, supports and fixture and mounting components are not included [13].
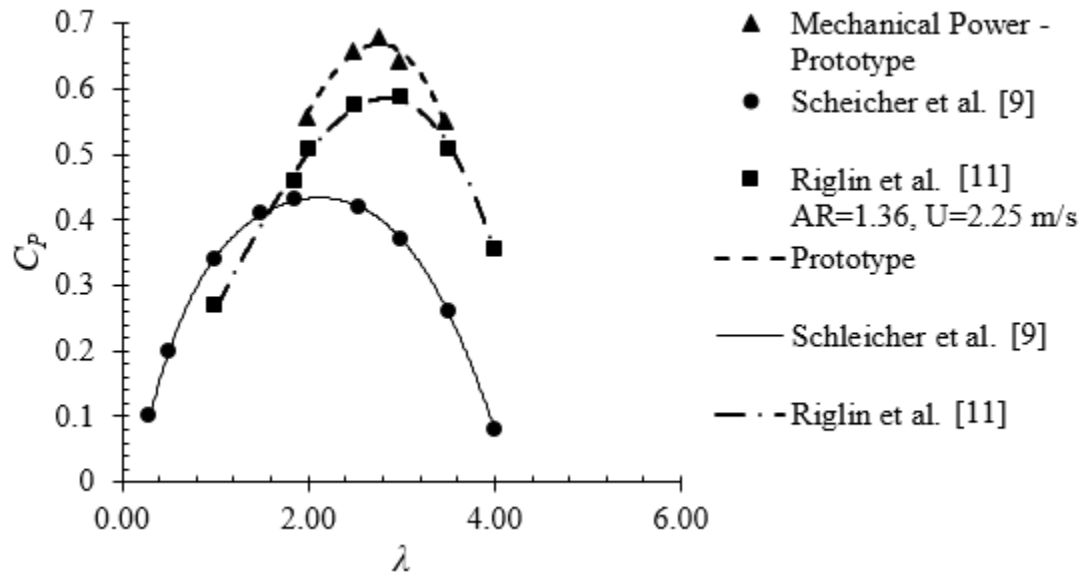
Figure 23. Power coefficient as a function of tip speed ratio from rapid CFD results [13]
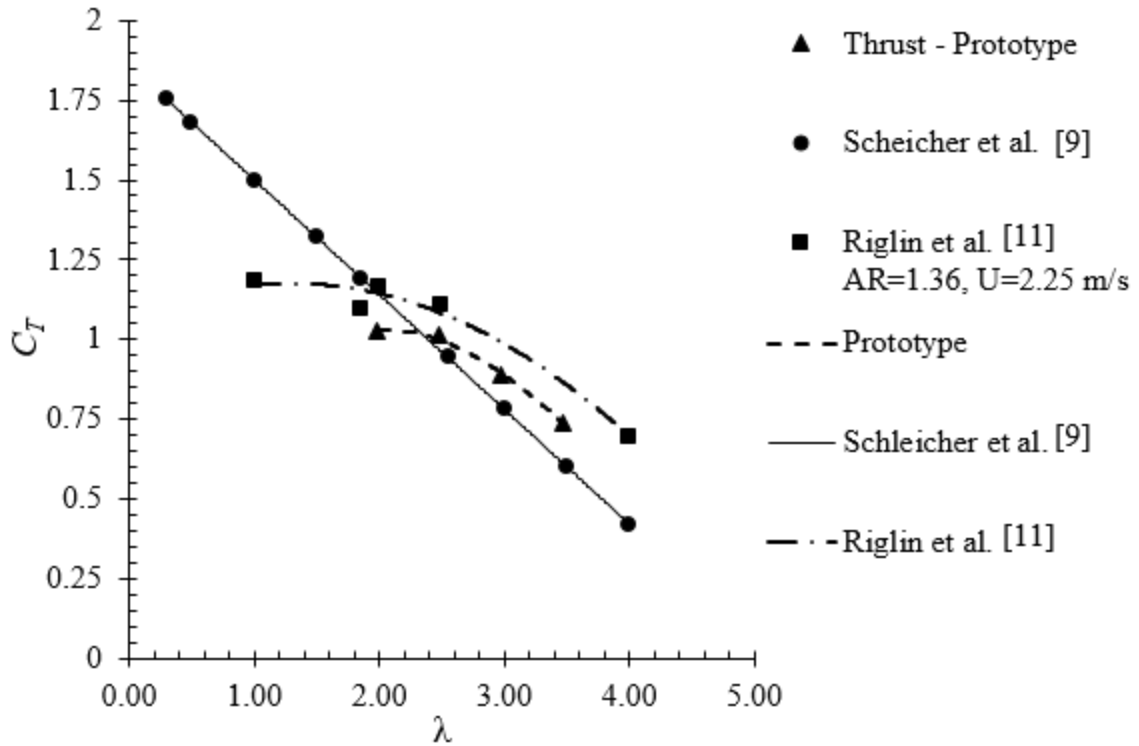
Figure 24. Coefficient of thrust as a function of tip speed ratio [13]

Experimental Results

Experiments were conducted at the Circulating Water Channel (CWC) at the Naval Surface Warfare Center, Carderock Division [16]. . Two, 14-gage copper wires were led from the generator to electrical monitoring and data acquisition equipment. Two primary experiments were conducted. The first experiment held a constant current to control the load on the generator for 2 minute intervals, increasing the current upon completion of each interval. The power produced was measure by a data logger each second during the time intervals. The second setup used a capacitor in conjunction with a Solar Charging Converter (SCC) to trickle charge a battery bank. The channel was operated at flow speeds ranging from 1.0 m/s to 1.7 m/s to determine the power production of the prototype.

Both numerical and experimental results yield approximately the same performance under peak conditions. The prototype was designed to operate around a tip speed ratio of 2.5. At tip speed ratios exceeding 2.5, the experimental results show a steep drop from predictions. The drop-off in power production can be attributed to the very steep power curve of the generator. This is only magnified by the 10:1 gear ratio selected for this application. The generator only functions properly at a small range of rotation rates due to the gear ratio optimized for flow rates of 1.5m/s.

Performance terms, including power, thrust (T), drag (D) and lift (L), of the modeled hydrokinetic turbine designs are normalized based on swept area (A), fluid properties, and upstream velocity. Performance and normalized terms are included below:

$$P = \tau \Omega \tag{18}$$

$$C_P = \frac{P}{\frac{1}{2}\rho A U^3} \tag{19}$$

$$C_T = \frac{T}{\frac{1}{2}\rho A U^2} \tag{20}$$

$$C_D = \frac{D}{\frac{1}{2}\rho A U^2} \tag{21}$$

$$C_L = \frac{L}{\frac{1}{2}\rho A U^2} \tag{22}$$

$$\lambda = \frac{\Omega R}{U} \tag{23}$$

Here: C_T is the thrust coefficient, C_D is the drag coefficient, and C_L is the lift coefficient, and λ is the tip speed ratio.
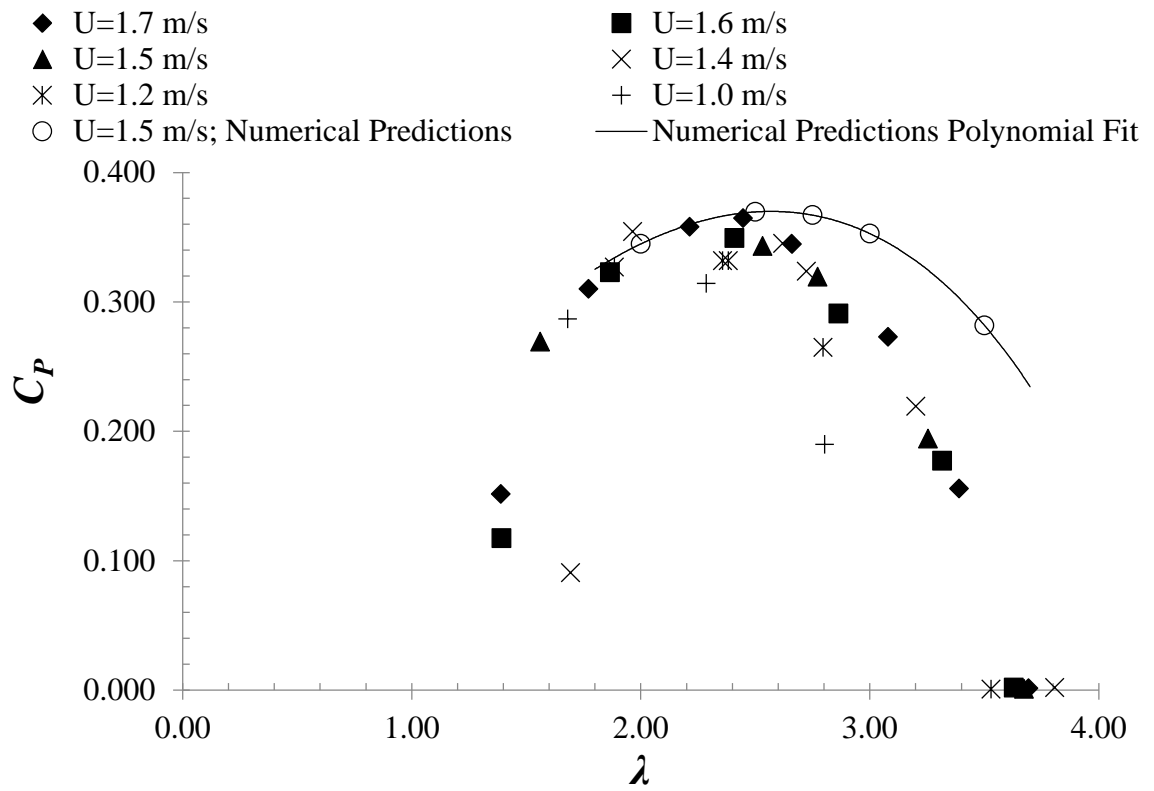
Figure 25 : Power coefficient as a function of tip speed ratio at various flow speeds [13]

Chapter 5: Conclusion

Key performance parameters of turbine units were introduced, including tip speed ratio, power coefficient, and thrust coefficient. These were the parameters used to optimize the blade geometry and diffuser geometry using numerical modeling techniques highlighted in Chapter 2. To verify the findings in [], a prototype was produce. The fabrication of the prototype required critical design changes and precautions due to the scale and location of testing.

The ideal operational conditions for each design parameter were experimentally explored. A tip speed ratio of 2.5, torque of 37.6 Nm, input RPM of 1150 via the gearbox to the generator, power generation of 244W, flow speed of 1.5 m/s, and power efficiency of 44% [3] were predicted for the given runner and diffuser geometry, not accounting for mechanical losses introduced by the fixture and electrical losses introduced by the test set up. At peak performance of the experimental results of a flow speed of 1.5m/s and tip speed ratio of 2.5, the turbine produced 221.4W with an overall efficiency of 36% [13]. Considering the combination of error associated with the numerical methods imposed, mechanical losses due to minor structural instabilities, bearing friction, electrical losses due to the data logging set up and error associated with data acquisition equipment, simulation and analysis of this hydrokinetic device was verified.

Various manufacturing and design techniques were utilized to maintain the overall performance of the turbine while mitigating cost and ensuring both stability and functionality. The meaningful data obtained in simulations is only valuable if it can be realized experimentally. Moreover, the experimental data is only valuable if it can be

applied in an economical manner. The barrier to entry in most hydrokinetic markets is more often than not an economical concern. Therefore, the ability to effectively apply design for manufacture principles is inherently as valuable to furthering the capabilities of hydrokinetic technology as theoretical advances in the field.

References

[1] D. R. Dunn, B. T. Fichman, S. Kaplan and P. Smith, "Primary Energy Production by Source November 2015," U.S. Energy Information Administration, Washington, D.C., 2015.

[2] P. Jacobson, "Assessment and Mapping of the Riverrine Hydrokinetic Resource in the Continental United States," Electric Power Research Institute (EPRI), Palo Alto, CA, 2012.

[3] J. Riglin, C. Daskiran, N. Oblas, W. Schleicher and A. Oztekin, "Design and Characteristics of a Micro-Hydrokinetic Turbine System," in *Proceedings of the International Mechanical Engineering & Exposition (IMECE2015)*, Houston, TX, 2015.

[4] J. Riglin, W. C. Schleicher and A. Oztekin, "Diffuser Optimization for a Micro-Hydrokinetic Turbine," in *ASME 2014 International Mechanical Engineering Congress and Exposition*, Montreal, Quebec, Canada, 2014.

[5] D. C. Wilcox, Turbulence Modeling for CFD, La Canada, California: DCW Industries, Inc., 2010.

[6] J. Boussinesq, "Theorie de l'Ecoulement Tourbillant," *Mem. Presentes par Divers Savants Acad. Sci. Inst. Fr.,* vol. 23, pp. 46-50, 1877.

[7] F. R. Menter, "Zonal Two-Equation k-ω Turbulence Models for Aerodynamic Flows," *AIAA Paper 93-2906.*

[8] F. R. Menter, "Two-Equation Eddy-Viscosity Turbulence Models for Engineering Applications," *AIAA Journal,* vol. 32, no. 8, pp. 1598-1605, 1994.

[9] R. Issa, "Solution of Implicitly Discretized Fluid Flow Equations by Operator Splitting.," *J. Comput. Phys.,* vol. 62, pp. 40-65, 1986.

[10] W. C. Schleicher, "Design Optimization of a Portable, Micro-hydrokinetic Turbine," Bethlehem, PA, 2014.

[11] J. Riglin, W. Schleicher, I. Liu and A. Oztekin, "Characterization of a micro-hydrokinetic turbine in close proximity to the free surface," *Ocean Engineering,* vol. 110, pp. 270-280, 1 December 2015.

[12] J. Riglin, W. C. Schleicher and A. Oztekin, "Numerical Analysis of a Shrouded Micro-Hydrokinetic Turbine Unit," *Journal of Hydraulic Research,* vol. 53, no. 4, pp. 525-531, 12 July 2015.

[13] J. Riglin, "Design, Modeling, and Prototyping of a Hydrokinetic Turbine Unit for River Application," Lehigh University, Bethlehem, PA, 2015.

[14] T. Matsushima, S. Takagi and S. Muroyama, "Characteristics of a highly efficient propeller type small wind turbine with a diffuserq," *Renewable Energy,* vol. 31, pp. 1343-1354, 2006.

[15] W. Schleicher, J. Riglin and A. Oztekin, "Numerical Characterization of a Preliminary Portable Micro-hydrokinetic Turbine Rotor Design," *Renewable*

Energy, vol. 76, pp. 234-241, 2015.

[16] H. Saunders and C. Hubbard, "The Circulating Water Channel of the David W. Taylor Model Basin," *SNAME Transactions,* vol. 52, 1944.

[17] W. Schleicher, J. Riglin and A. Oztekin, "Numerical Optimization of a Portable Hydrokinetic Turbine," in *Marine Energy Technology Symposium*, Seattle, WA, 2014.

Appendix A: Generator Specs and Dimensions

<u># 443905 Permanent Magnet DC Generator</u>

Maximum charging current for this generator is 20A. For continuous duty the generator should be run at 10A charging current or below.

Current Rating:

20A – 20 minutes max
15A – 50 minutes
10A or below – **continuous duty**

Please note: This generator is not designed for direct outdoor use, in rain or submerged in water. If used outside, it must be housed in an enclosure, appropriately sealed for outdoor use.

*Generators are non- returnable once installed and connected to a power supply.*

If you receive a generator that is damaged in shipping, please notify us immediately at 802-425-3435 - before you install the generator into your application.

Windstream Power LLC
802-425-3435

1.   Check for damage to the packaging or to the generator itself.

2.   With the output wires separated, turn the shaft by hand. A slight resistance will be
            felt, due to new brush and bearing friction. *As the bearings and brushes are "run
            in" over a period of time, this friction will be reduced.*

3.   Now touch the output wires together, and again turn the shaft. It should now be
            much more difficult to turn the shaft, due to "magnetic braking".

f there is any apparent damage, or if any of these tests do not work, notify the shipping
company who delivered the generator, and notify the dealer from whom you purchased the
generator. All generators are inspected before shipping, and are fully insured against damage.

GENERATOR CONNECTIONS, APPLICATIONS AND ACCESSORIES
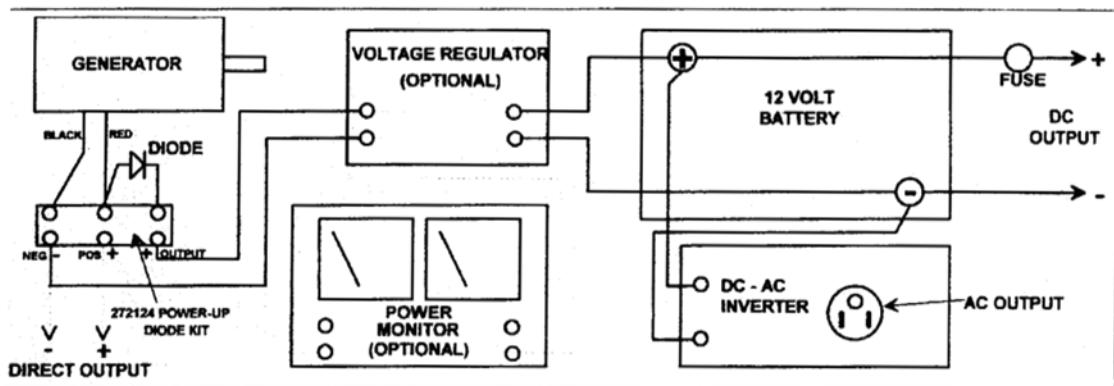
The red output wire is POSITIVE (+)   **The black output wire is NEGATIVE (-)**

While looking at the end of the generator shaft, turn the shaft in a clockwise direction to obtain the
ndicated polarity. Turned counterclockwise, the black wire would then be positive and the white
negative. The generator can be turned in either direction without damage. The polarity can also be
reversed, if desired, by disassembling the generator and rotating the magnet drum through 180
degrees.

To obtain the same polarity from rotation in either direction, connect the generator output wires to the ac
connections on a full wave rectifier bridge, such as the 272125 bridge kit. The output of the + and -
connections of the bridge will be the same polarity for either direction of rotation of the generator shaft.

Wire nuts or any other means can be used instead of a barrier strip to make the generator conections.
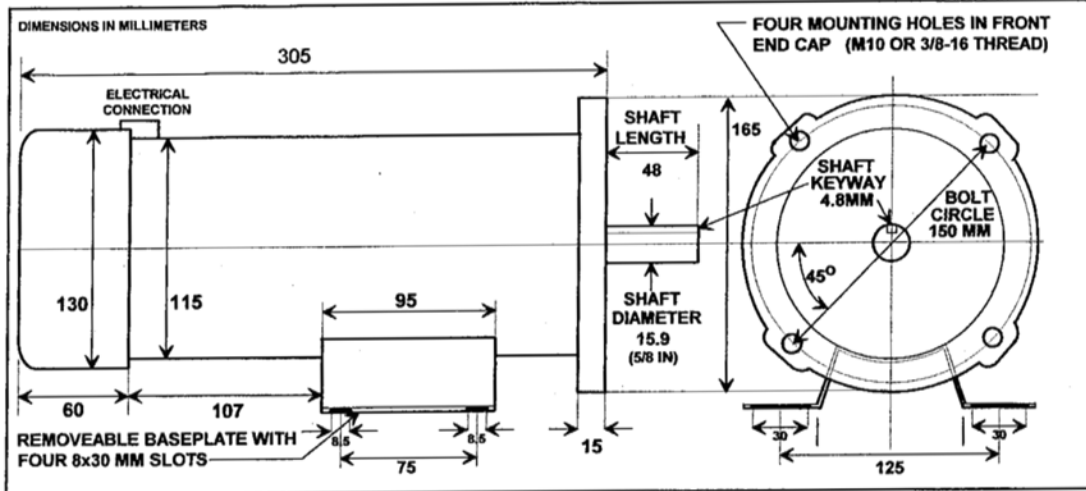
The arrow or band (cathode) on the reverse-current diode should be on the side away from the
generator. The purpose of this diode is to prevent the battery from turning the generator like a motor.

Replacement brushes, bearings or other parts, as well as diodes, regulators, power monitors, batteries
and inverters can be obtained from Windstream.

LOW RPM PERMANENT MAGNET DC GENERATOR
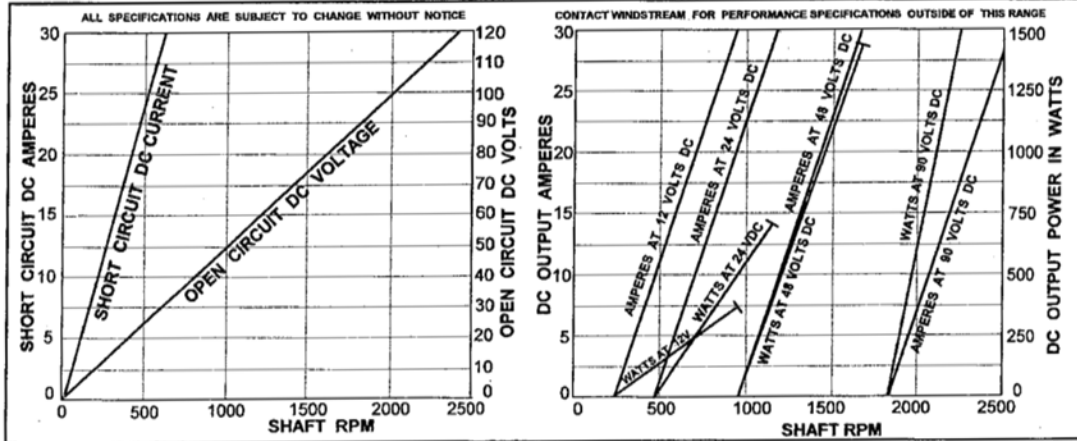## STOCK NO. 443905

...TECH

DIMENSIONS IN MILLIMETERS

FOUR MOUNTING HOLES IN FRONT END CAP (M10 OR 3/8-16 THREAD)

305

ELECTRICAL CONNECTION

SHAFT LENGTH 48

165

SHAFT KEYWAY 4.8MM

BOLT CIRCLE 150 MM

130 115

95

45°

SHAFT DIAMETER 15.9 (5/8 IN)

60 107

REMOVEABLE BASEPLATE WITH FOUR 8x30 MM SLOTS

8.5 8.5

75

15

30 30

125

MECHANICAL SPECIFICATIONS

Overall length	305mm (12in)	Faceplate diameter	165mm (6.5in)
Weight	12.6kg (27.6 lb)	Shipping weight	14kg (31 lb)
Magnet drum diameter	115mm (4.5in)	Shaft keyway	4.8mm (3/16in)
Shaft diameter	15.9mm (5/8in)	Shaft length	48mm (1.9in)
Maximum shaft speed	3,000 rpm (50 Hertz)	Rotation	Either direction (Polarity reverses)

Mounting	Four tapped holes on 150mm bolt circle in front end cap, or by removeable baseplate.
Bearings	Two sealed ball bearings - bore 17, width 12, 40 mmOD - Replacement bearing stock no. 171109.
Armature	76.4mm OD, stack length 152mm, 21 slots, skewed laminations to minimize cogging. Series wound, 42 segment commutator.
Magnets	Two saturated C8 annular ceramic magnets 12mm thick by 164mm long.
Brushes	Extra-large 19mm wide by 25 long. - Replacement brush assembly stock no. 443730.

ELECTRICAL SPECIFICATIONS

Output voltages	12, 24, 36, 48, 90 or 120 (determined by load and rpm).
Output current	30 amperes maximum. Armature windings 1mm (AWG18) magnet wire (fusing current 82 amps).
Ouput power	3.6kW maximum, operating at 120 volts (4.8hp). Ratings are determined by the operating voltage. High current operation requires cooling.

Internal resistance	1.1 ohms	Inductance	4.8mH

PERFORMANCE

443905 - NOVEMBER 2002

ALL SPECIFICATIONS ARE SUBJECT TO CHANGE WITHOUT NOTICE

CONTACT WINDSTREAM FOR PERFORMANCE SPECIFICATIONS OUTSIDE OF THIS RANGE

TROUBLESHOOTING GUIDE FOR PERMANENT MAGNET DC GENERATORS

If there is too much resistance to turning the generator:

1. Completely disconnect the generator (both wires)
If the resistance disappears, there was a load or a short circuit in the external wiring.

2. If the resistance is still present, unscrew the brusholders and remove the brushes.
If the resistance disappears, there is excessive brush pressure, such as caused by a nearly-worn-out brush catching on a commutator segment and getting jammed, or the brush has somehow become gummed up, or debris such as a magnet fragment has got in between the brush and the commutator.
To correct, inspect the brushes, replace one or both if necessary, or brush and blow out around the commutator.

3. If the resistance is still present, determine whether the resistance is constant or varying as the shaft is turned.
If the resistance is varying - dragging at certain points as the shaft is turned - then there is probably one or several short circuits in the armature winding, caused by overheating, resulting in the enamel insulation melting and the windings contacting each other. If this is the problem, the armature or complete generator has to be replaced.
If the resistance to turning is constant as the shaft is turned, the cause is likely failure of one or both bearings. Typically the front bearing can fail prematurely if the generator is operated with excessive side pressure, such as from a too-tight v-belt.
To correct, disassemble the generator, remove the armature, determine which bearings are hard to turn, and replace them.

4. Occasionally, a generator can be disabled by a fragment of magnet breaking off and lodging between the edge of a magnet and an armature segment. If this happens, disassemble the generator and remove the fragment, and also clean out any other such fragments, which will be adhering strongly to the magnets.

Call Windstream Power LLC for parts and repair 802-425-3435

EFFICIENCY IN SMALL PERMANENT MAGNET DC GENERATORS

The overall efficiency of small permanent magnet dc generators is determined by several independent factors, so there is no single efficiency figure that can be specified for any particular generator. Efficiencies range from 75% to 95%, with a mean of about 85%.

Efficiency is affected by the following factors:

1. **Magnet type and strength** - low cost generators use ceramic C8 magnets, and higher cost, higher efficiency generators use neodymium ("rare earth") magnets.

2. **Magnetic gap** - the smaller the clearance between armature poles and magnets, the better the magnetic flux path and the higher the efficiency (but also see "windage" in item 5 below).

3. **Winding resistance** - the lower the internal electrical resistance of the winding, the less energy is dissipated as heat that results from current flow through the winding resistance. Accordingly, the larger the magnet wire diameter in the armature windings, the lower the resistance and the higher the electrical efficiency, but the larger the generator (the same number of turns of the larger wire gauge are required to generate the same output voltage). The internal resistance and wire gauge is given in the specifications of each generator type.

4. **Heat** - both ambient heat and heat generated by current flow through the windings - the higher the temperature, the higher the resistance and the lower the efficiency. Air cooling of windings, both convective and forced air, improves the generator efficiency.

5. **Windage** - the resistance to rotation caused by air friction around the rotating armature - is higher for very narrow magnetic gaps, and is also higher at higher shaft rpms as well as larger armature diameters.

6. **Load characteristics** - the nature of the generator load, a completely external factor, influences the overall efficiency. Generally, the maximum efficiency occurs when the source (generator) impedance is matched to the external load impedance. In dc generators, impedance effects occur when the inductance of the generator windings interacts in any way with the load. A non-inductive load such as a battery or a resistance heater can be considered purely resistive, while the generator impedance is then simply its internal dc resistance.

Given that the final precise efficiency of a dc generator in a particular application is affected in some way by all the above factors - rpm, load characteristics, internal resistance, voltage, power output and temperature, as well as generator size, magnet type and magnetic gap, the only way to determine the exact efficiency is to measure it in the application and conditions it is to be used. If the input torque and rpm are known or can be measured, and the output power measured at the steady-state loaded temperature, in those conditions, the efficiency is simply the quotient of input over output power:

Calculation of efficiency E - efficiency $E = \dfrac{P_{OUT}}{P_{IN}}$ (E x 100 = percent efficiency)

The input power P_{IN} = 6.28 x shaft torque T (in Newton-meters) x rotational frequency f (in Hertz or revolutions per second). If the rotational frequency is in rpm, multiply by 60.

The output power P_{OUT} in watts = output voltage V_O x output current I_O as measured by a voltmeter and ammeter.

Understanding Output Voltage, Current and Power with Permanent Magnet DC Generators

The output voltage of a permanent magnet dc generator depends on the shaft rpm and the load. All Windstream permanent magnet generators will operate at any voltage within the operating envelope indicated on the published specifications. **The rpm required to reach any particular voltage is determined by the load** - the lighter the load, the lower the rpm needed to reach the specified voltage.

We have performance curves for each generator to show the rpm vs. load relationship. One of the curves shown in the specifications is the no-load (open-circuit) voltage, and the other curve is the short-circuit current. The performance at any load and rpm can be calculated knowing these factors plus the internal resistance of the generator.

An example of a battery charging application (24V)

The float voltage of a 24 volt battery is typically 27.6 volts. By controlling the generator rpm, it can be made to deliver 27.6 volts, or in the case where the input rpm is variable, such as from a wind turbine, a 24 volt voltage regulator can be used to limit the output voltage to the battery to 27.6 volts, no matter what the rpm (within the operating ranges of the generator and regulator).

When charging a battery with a permanent magnet dc generator, the generator rpm first has to rise to the point where its output voltage reaches the battery terminal voltage - a discharged 24 volt battery might have a terminal voltage of 20 or so. As soon as the generator exceeds that voltage, current starts to flow into the battery, and the effort required to turn the generator (i.e. input torque) increases. **As long as that amount of torque can be supplied by whatever is turning the generator, the battery will continue to charge.**

As soon as the battery becomes fully charged, no more charging current will flow, and the load disappears. If the generator continues to be driven, then the output voltage, with no load, will rise, and that could damage the

51

battery unless limited by a voltage regulator, or by disconnecting the generator when the charging current drops to zero or the battery terminal voltage reaches 27.6.

When charging a battery from a permanent magnet dc generator, it is also necessary to insert a diode into the charging circuit so that, if the generator rpm drops, the battery does not start to turn the generator like a motor, which discharges the battery. This is particularly important with variable power sources like wind turbines or human power generators. The diode acts like a one-way valve, allowing current to pass into the battery but not out. A voltage regulator includes an internal diode, so no additional diode is needed when using a voltage regulator.

Current and RPM when connected to a load

The current ("amperage") of a dc generator at any rpm is governed **only** by the load put on it, not by its rpm - **if you run a generator with no load, the current stays at zero no matter how high the rpm**. Only the generator terminal voltage goes up, but no matter how high the voltage, if there is no load, there is no current flow.

So the only limitation on rpm on a low rpm generator, as long as the current is kept within the limit for that generator, is if it is turned so fast with no load that the voltage rises so high that it could arc from one commutator segment to the next. As long as there is a load, preventing the voltage from rising to the arcing level, you can use a dc generator at any rpm you want.
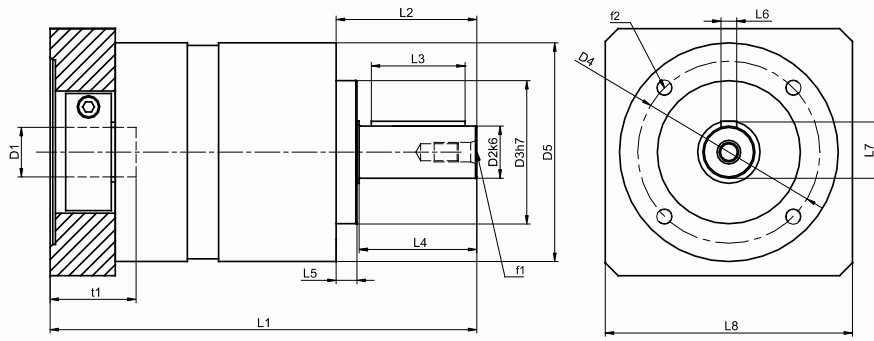
Appendix B: GAM PE-W Series Gearbox

he PE Series gearboxes to meet your needs. Page 4 provides a list of commonly requested modifications to give you a feel for our capabilities.

PE-N (with EKC)

PE-W

Vita

Nicholas Tyler Oblas was born April 9th, 1992 in Bethlehem, Pennsylvania. Nick grew up in Hellertown, PA and attended Saucon Valley Senior High School. He played football for 4 years while growing a passion for mathematics and the physical sciences. The pursuit of an engineering degree was ultimately derived from a burning curiosity of how everything and anything works from my father, cultivated by a passionate math teacher, Mr. Kipp who managed to spark a love for mathematics in a high school student from a small town.

Nick enrolled at Lehigh University in 2010 in the Mechanical Engineering department where he joined a fraternity, played club soccer, conducted undergraduate research, and ultimately started PSO Consulting, LLC, an engineering design firm with two Lehigh classmates. Nick completed his Master of Science in Mechanical Engineering in January 2016.